JGR Oceans

RESEARCH ARTICLE

10.1029/2021JC018095

Key Points:

- Observed overtides are useful in selecting the optimal bathymetry and constraining parameters of ocean models in tidally dominated regions
- They can also be used to validate, and physically interpret, mean dynamic topography predicted by ocean models
- Overtides are useful in the design of geodetic and ocean observing systems in tidally dominated regions

Supporting Information:

Supporting Information may be found in the online version of this article.

Correspondence to:

C. Renkl,
christoph.renkl@dal.ca

Citation:

Renkl, C., & Thompson, K. R. (2022). Validation of ocean model predictions of mean dynamic topography in shallow, tidally dominated regions using observations of overtides. *Journal of Geophysical Research: Oceans*, *127*, e2021JC018095. https://doi.org/10.1029/2021JC018095

Received 2 OCT 2021
Accepted 14 FEB 2022

Validation of Ocean Model Predictions of Mean Dynamic Topography in Shallow, Tidally Dominated Regions Using Observations of Overtides

C. Renkl[1] and K. R. Thompson[1]

[1]Department of Oceanography, Dalhousie University, Halifax, NS, Canada

Abstract In shallow, tidally dominated regions, overtides and the mean state of the ocean are coupled through their simultaneous generation by nonlinear processes. We present a new method that uses observed overtides (e.g., M_4) and mean currents to independently assess the accuracy of mean dynamic topography (MDT) predicted by ocean models. This is useful in regions where no sufficiently long, geodetically referenced sea level records are available for validation of the predicted MDT. We apply the new method to a regional model of the Gulf of Maine/Scotian Shelf region (GoMSS) and a barotropic, higher resolution model focused on the upper Bay of Fundy (UBoF). We first show that the tides and mean circulation predicted by UBoF are in good agreement with observations and a significant improvement over GoMSS. Next, we use UBoF to demonstrate that observed overtides are useful in selecting the optimal bathymetry and constraining parameters of an ocean model. An accurate bathymetry is critical for capturing the dominant nonlinear processes that generate overtides and control the form of MDT in shallow, tidally dominated regions. Finally, we use the observed overtides to argue that the MDT predicted by UBoF is more realistic than the prediction by GoMSS. In the vicinity of headlands, both horizontal advection and bottom friction in UBoF generate harmonics of the tidal flow and local setdowns of coastal MDT of $\mathcal{O}(10\text{ cm})$. The prediction of such features, validated by observed overtides, can provide guidance in future deployments of tide gauges in support of geoid and ocean model validation.

Plain Language Summary Overtides are higher harmonics of the main astronomical tidal constituents. They are often observed in shallow, tidally dominated regions and are dynamically linked to spatial variations in the mean state. In this study, we use observed overtides to compare predictions by a regional model of the Gulf of Maine/Scotian Shelf region (GoMSS) and a simpler, but higher resolution, model of the upper Bay of Fundy (UBoF). It is first shown that the tides and mean circulation predicted by UBoF are in good agreement with observations and a significant improvement over GoMSS. UBoF is then used to demonstrate that observed overtides are useful in optimizing the configuration of ocean models, including the representation of the sea floor. We next show that observed overtides can be used to assess the accuracy of the mean state predicted by ocean models, including spatial variations in mean sea level. An advantage of this approach is that overtides can be estimated from short records of sea level and currents thereby increasing the number of locations at which models can be assessed. Finally, we argue that ocean models validated using overtides can provide guidance in the design of geodetic and ocean observing systems in tidally dominated regions.

1. Introduction

Mean dynamic topography (MDT) is the height of the mean sea level above the geoid after removal of the inverse barometer effect (e.g., Hughes & Bingham, 2006). The MDT includes contributions from spatial changes in sea water density, mean setup due to local winds, and nonlinear processes such as the Bernoulli setdown (Batchelor, 1967) due to tidal currents around headlands. In the open ocean, mean surface currents are approximately in geostrophic balance leading to a simple relationship between MDT and mean surface circulation. The interpretation of alongshore changes in MDT becomes more subtle approaching the coast because the geostrophic balance is no longer dominant in the alongshore direction and frictional processes become more important (e.g., Higginson et al., 2015; Hughes et al., 2019; Lentz & Fewings, 2012).

Despite the subtlety of the alongshore momentum balance, it is still useful for practical applications. A particularly simple illustration is provided by considering a constant density ocean in a rectangular basin of constant depth lying on a mid-latitude β-plane. If the ocean circulation is forced by a steady, purely zonal wind stress varying with latitude, the meridional Sverdrup flow integrated across the basin is balanced by a return flow in a narrow western boundary current (e.g., Munk, 1950; Stommel, 1948). It is straightforward to show, using simple vorticity arguments, that the tilt of MDT along the western coastal boundary is proportional to the meridional transport of the boundary current and independent of the details of the frictional dissipation in the model (e.g., Thompson et al., 1986). Stewart (1989) showed that this extends to inertial western boundary layers.

Estimates of MDT along the coast, with standard errors typically less than 3 cm, can now be made using long tide gauge records and the latest generation of geoid models (henceforth the geodetic approach; Huang, 2017; Woodworth et al., 2012). These new estimates have proved useful in validating predictions of alongshore variations of MDT by ocean models (henceforth the hydrodynamic approach) and also their predictions of mean circulation on both basin and global scales (e.g., Higginson et al., 2015; Lin et al., 2015; Woodworth et al., 2012). Agreement between MDT predicted by the geodetic and hydrodynamic approaches increases confidence in both the geoid and ocean models.

The geodetic approach to estimating coastal MDT is limited to locations where decades of sea level observations, made by tide gauges with continuous vertical datum control, exist. This limits severely the number of locations at which the geodetic approach can be used. Here, we propose a fundamentally different approach to evaluate model predictions of coastal MDT using observations of overtides (higher harmonics of the main astronomical tidal constituents; e.g., Le Provost, 1991). This approach has two important advantages: it does not require information about the geoid and it can be applied to relatively short, $\mathcal{O}$(1 month), sea level records, thereby greatly increasing the number of locations at which the ocean models can be validated.

Overtides are generated primarily by nonlinear processes involving sea level and currents, for example, horizontal advection and dissipation by bottom friction. They have been studied extensively using analytical and numerical models as well as observations (e.g., Aubrey & Speer, 1985; Friedrichs & Aubrey, 1988; Le Provost, 1991; Parker, 1991; Pingree & Maddock, 1978; Speer & Aubrey, 1985). Comparing observed and predicted overtides provides information about the ability of ocean models to capture these dominant nonlinear processes (Pingree & Maddock, 1978). It has been shown that the same nonlinear processes can have a direct influence on mean sea level (e.g., Li & O'Donnell, 1997, 2005; Pingree et al., 1984). This raises the possibility of validating the mean state of an ocean model by assessing the accuracy of its predicted overtides.

The initial motivation for the present study was the need to assess the realism of a large (~10 cm) setdown of MDT in the upper reaches of the Bay of Fundy predicted by the Gulf of Maine and Scotian Shelf model (GoMSS; Katavouta & Thompson, 2016). Based on theoretical considerations (e.g., Li & O'Donnell, 1997, 2005), we expected a small setup of a few centimeters. Unfortunately, no long, geodetically referenced, tide gauge records were available for the study region. This encouraged us to explore the use of overtides in the validation of the predicted setdown.

The Bay of Fundy, together with the Gulf of Maine, is a near-resonant system with an extreme tidal range at the M_2 tidal frequency (Garrett, 1972). The present study will focus on Minas Channel, Minas Basin, and Cobequid Bay (Figure 1) where the highest tides in the world have been observed. In such shallow, tidally dominated regions, the largest overtide is expected to be the first harmonic M_4 (Speer et al., 1991). For reference, the periods of M_2 and M_4 are 12.42 and 6.21 hr, respectively.

The tidal dynamics and mean circulation of the Bay of Fundy have been the subject of numerous modeling and observation programs (e.g., Dupont et al., 2005; Greenberg, 1983; Hasegawa et al., 2011; Karsten et al., 2008; Tee, 1977; Wu et al., 2011). Many of these earlier studies were motivated by the need for reliable assessments of the impact of tidal energy extraction, including the effect on near and far field sediment transport. However, the MDT of the region has not been investigated.

The approach described in this study has wider applicability than just checking the accuracy of the MDT predicted by GoMSS in the Bay of Fundy. From an oceanographer's perspective, this study justifies the use of overtides in the validation of the mean state predicted by ocean models in tidally dominated regions. From a geodesist's perspective, an ocean model that has been validated using observed overtides is a potentially more reliable tool for assessing geoid models in tidally dominated regions. The same ocean model can also be used with more

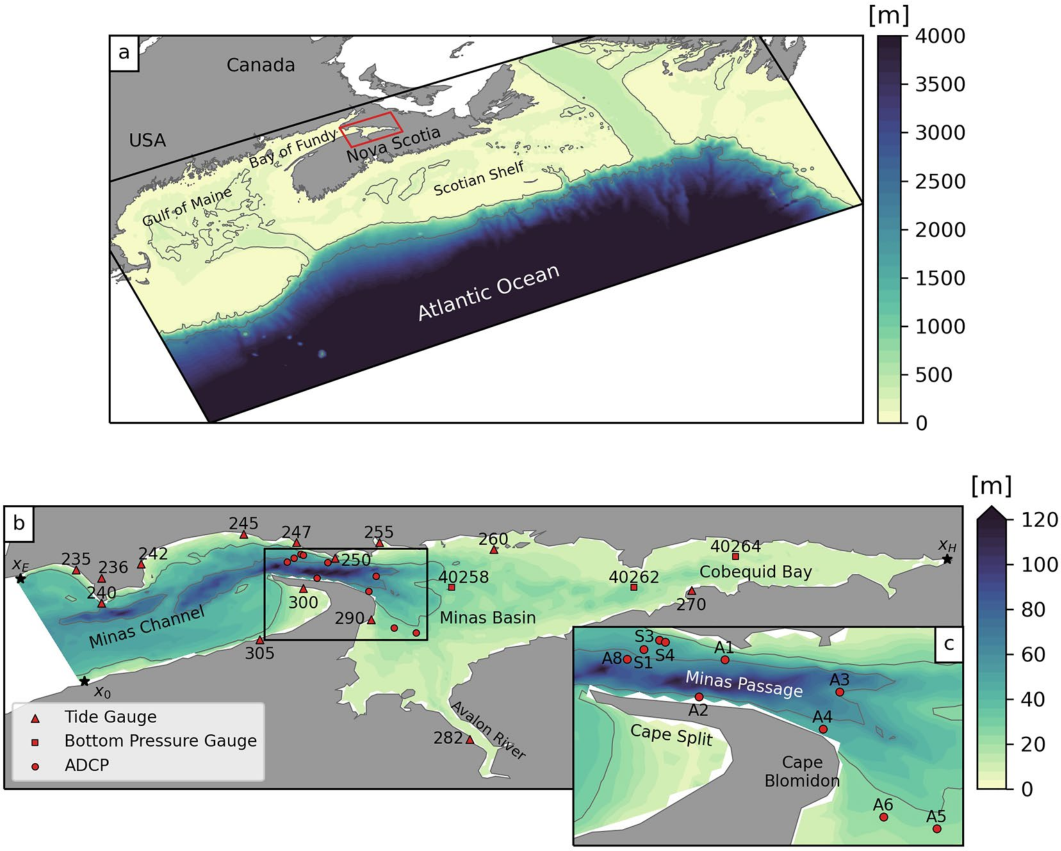

Figure 1. Model domains and observation locations. (a) Model domain and bathymetry of the Gulf of Maine/Scotian Shelf model; contours indicate the 200 and 2,000 m isobaths. The red rectangle defines the model domain of upper Bay of Fundy (UBoF) which is shown in detail in panel (b) where contours mark the 30 and 60 m isobaths. Triangles and squares show the positions of the tide gauges and bottom pressure gauges, respectively, used in this study. Circles mark the locations of Acoustic Doppler Current Profiler measurements. Black stars are alongshore reference points used throughout this study. (c) Enlarged view of the UBoF model domain in the vicinity of Cape Split (see black rectangle in panel b).

confidence to select the location of tide gauges for future long-term measurements of sea level in support of geoid model validation, and also correcting existing mean sea levels for localized oceanographic effects.

Based on the above discussion, the following three questions will be addressed with particular emphasis on the upper Bay of Fundy. In tidally dominated regions, how useful are observed overtides in (a) selecting the optimal bathymetry for an ocean model, and constraining the model's parameters? (b) validating model predictions of MDT? (c) designing geodetic and ocean observing systems?

The structure of this study is as follows. Section 2 provides a brief overview of the generation of overtides and their relationship to MDT with particular attention paid to tidal flow through channels and past headlands. Both of these flow regimes play an important role in shaping the MDT in the Bay of Fundy. In Section 3, the GoMSS model is described and a high-resolution model for the upper Bay of Fundy is introduced. Section 4 describes the observations used in Section 5 to validate the ocean models introduced in Section 3. The predicted MDT is described in Section 6 along with its sensitivity to horizontal resolution, bathymetry, lateral viscosity, and bottom friction parameters. The results are summarized and discussed in Section 7.

2. Background and Theory

This section provides the theoretical background required to justify the use of overtides in the evaluation of ocean model predictions of the mean state with a particular focus on MDT. Following a general discussion of the generation of overtides, two situations of particular relevance to the present study are discussed: tidal flow around a headland and along a narrow channel closed at one end.

The underlying momentum and continuity equations are taken to be (Robinson, 1983):

$$\frac{\partial \mathbf{u}}{\partial t} + \mathbf{u} \cdot \nabla \mathbf{u} + f\hat{\mathbf{k}} \times \mathbf{u} = -g\nabla\eta - c_{\mathrm{d}}\frac{\mathbf{u}\,|\mathbf{u}|}{h} + A_{\mathrm{h}}^{\mathrm{m}}\nabla^2\mathbf{u}, \tag{1}$$

$$\frac{\partial \eta}{\partial t} + \nabla \cdot (h\mathbf{u}) = 0. \tag{2}$$

Here, $\mathbf{u}(\mathbf{x}, t) = u\hat{\boldsymbol{\imath}} + v\hat{\boldsymbol{\jmath}}$ is the horizontal current averaged over the total water depth

$$h = H + \eta, \tag{3}$$

Where H is the water depth at rest and η is the height of the sea surface above the geoid. The horizontal unit vectors $\hat{\boldsymbol{\imath}}$ and $\hat{\boldsymbol{\jmath}}$ are perpendicular to the orientation of local gravity indicated by the unit vector $\hat{\mathbf{k}}$. f is the Coriolis parameter and g is the vertical acceleration due to gravity. A quadratic bottom friction law is assumed with constant drag coefficient c_{d}. $A_{\mathrm{h}}^{\mathrm{m}}$ is the horizontal eddy viscosity coefficient. Atmospheric forcing and density variations have been ignored along with terms that arise from the vertical shear of the current on depth-averaging the horizontal advection term (Robinson, 1983).

The momentum Equation 1 has two nonlinear terms related to horizontal advection and bottom friction. The continuity Equation 2 has a single nonlinear term involving the product of η and $\mathbf{u}$. If the system is forced by a single tidal constituent, all three terms can individually generate both overtides and a change in the mean state (e.g., Parker, 1991). As will be discussed below, the relationship between overtides and the mean state is not straightforward and depends on the nonlinearities that generate them (e.g., Pingree et al., 1984).

The vorticity equation can provide physical insights into the generation of overtides. The curl of Equation 1 leads to the following equation governing the evolution of relative vorticity ζ (e.g., Signell & Geyer, 1991):

$$\frac{\partial}{\partial t}(f + \zeta) + \mathbf{u} \cdot \nabla (f + \zeta) = \frac{(f + \zeta)}{h}\mathbf{u} \cdot \nabla h - \hat{\mathbf{k}} \cdot \nabla \times \left(c_{\mathrm{d}}\frac{\mathbf{u}\,|\mathbf{u}|}{h}\right) + A_{\mathrm{h}}^{\mathrm{m}}\nabla^2\zeta. \tag{4}$$

The terms on the right-hand side of 4 correspond to changes in ζ due to vortex tube stretching, and torques involving bottom stress and lateral friction. The bottom friction term can be decomposed in a dissipation term and two generation terms associated with spatial changes in water depth and current speed (Signell & Geyer, 1991). The vorticity equation will prove useful in the following discussion of flow around headlands, and also the interpretation of MDT.

2.1. Tidal Flow Around a Headland

In a seminal study of tides in the Bay of Fundy, Tee (1976) used a numerical model based on Equations 1 and 2 to show how the combined effect of vorticity generation and its subsequent advection could generate strong mean flows in the vicinity of headlands with speeds approaching 1 $\mathrm{m\,s^{-1}}$. The predictions by the model were subsequently shown to agree well with current measurements (Tee, 1977). Similar results have been found for other locations and it is now generally accepted that strong tidal flow past a headland can lead to flow separation and two permanent, counter-rotating eddies on each side of the headland that drive a mean flow along the coast toward the tip (e.g., Geyer & Signell, 1990; Pingree & Maddock, 1977; Robinson, 1983). It has also been shown that tidal flow past a headland can generate overtides in addition to a mean flow (Geyer & Signell, 1990; Mardell & Pingree, 1981).

Signell and Geyer (1991, hereafter SG91) used a combination of analytical and numerical models based on Equations 1 and 2 to examine the formation and evolution of transient eddies generated by tidal flow past an idealized headland. As a first step, SG91 used an analytical model to determine the conditions under which the flow separates from the coast (see their section 3.2). In this model, they assumed an elliptically shaped headland protruding from the x-axis and a thin shoaling region around it where the water depth decreases linearly toward the coast. Using boundary layer techniques, they argued that, in the absence of flow separation, the pressure gradient along the coast can be approximated by

$$g\frac{\partial\eta}{\partial s} = -\frac{\partial u_1}{\partial t} - u_1\frac{\partial u_1}{\partial s} - c_{\mathrm{d}}\frac{U_0 u_1}{H}, \tag{5}$$

Where s is the alongshore coordinate and $u_1(s, t)$ is the tidal current along the coast. To specify u_1 they assumed a large-scale irrotational flow, varying in time with tidal frequency ω as $\sin(\omega t)$. SG91 gave an analytic expression for $u_1(s, t)$ that satisfies the coastal boundary condition of no normal flow and approaches $U_0 \sin(\omega t)$ with increasing distance from the headland. Substituting the expression for $u_1(s, t)$ into Equation 5 resulted in an analytic expression for the time varying pressure gradient along the coast of the headland. SG91 used this pressure gradient to determine the location, and stage of the tide, at which the pressure gradient was adverse (i.e., increasing pressure in the downstream direction) leading to possible flow separation.

Equation 5 has one nonlinearity related to advection that leads to a Bernoulli setdown of sea level, $u_1^2/2g$. The tidal current u_1 is a separable function of location and time, so we can write $u_1(s, t) = U_1(s)\sin(\omega t)$. As a result, the Bernoulli setdown can be expressed as a local change in mean sea level and an overtide of sea level varying at twice the frequency of the tidal forcing:

$$\frac{u_1^2}{2g} = \frac{U_1^2}{2g} - \frac{U_1^2}{2g}\cos(2\omega t). \tag{6}$$

It follows that if one were to determine the overtide in sea level, it would be possible to also determine the mean Bernoulli setdown. A typical tidal current near a headland in the Bay of Fundy is $U_1 = 1.5\ \mathrm{m\,s^{-1}}$. This results in both an M_4 amplitude in sea level, and a mean Bernoulli setdown of about 10 cm. Bernoulli setdown provides a particularly simple demonstration of how knowledge of overtides can provide information about MDT.

As the strength of the large-scale tidal flow (U_0) increases (see SG91 for conditions), the momentum balance in Equation 5 eventually breaks down due to flow separation. SG91 used a numerical model, based on a discretization of Equations 1 and 2, to examine the generation and movement of the transient eddies generated by the oscillating flow past the headland. They showed that relative vorticity is primarily generated by bottom friction in the shoaling region around the headland and subsequently transported into the interior where it dissipates over a tidal cycle. After the tide reverses, the same mechanism injects relative vorticity of the opposite sign on the other side of the headland. As a consequence, the mean circulation is characterized by a pair of counter-rotating eddies on either side of the promontory consistent with the results of Tee (1976). These eddies drive a mean flow along both sides of the headland toward the tip.

The mean Bernoulli setdown in the numerical model of SG91 is greatest at the tip of the headland where the tidal current is strongest. In order to drive the mean coastal flow toward the tip of the headland, an additional setdown of sea level is needed to provide an alongshore pressure gradient to overcome friction. (The coastal boundary condition of no normal flow eliminates the Coriolis term.) More quantitatively, the mean sea level gradient required to overcome the friction opposing the time mean current $\overline{u}$ can be approximated by $\lambda\overline{u}/gH_0$, where $\lambda = 8c_{\mathrm{d}}U_1/3\pi$ is a linear drag coefficient (e.g., Proudman, 1953), and H_0 is the water depth near the coast. Taking typical values for the Bay of Fundy of $c_{\mathrm{d}} = 2.50 \times 10^{-3}$, $\overline{u} = 0.3\ \mathrm{m\,s^{-1}}$, and $H_0 = 10$ m gives a gradient in mean sea level along the coast of 10 cm over 10 km. This is in the same order as the Bernoulli setdown. We will see exactly this type of feature in the predicted MDT for the upper Bay of Fundy.

2.2. Tidal Flow Along a Narrow Channel

It is well known (e.g., Li & O'Donnell, 1997, 2005; Parker, 1991; Pingree et al., 1984) that the nonlinear terms in Equation 1 can generate a mean circulation in a narrow channel closed at one end. Li and O'Donnell (2005) used a perturbation technique to analyze the effect of channel length on the mean circulation in tidally dominated channels with lateral depth variations. They showed that mean sea level over a tidal cycle always increases toward the head of the channel when forced at the mouth by a tide with a single frequency. They explained this setup in terms of the superposition of an incident and reflected wave that are both attenuated by bottom friction. Because the travel path of the reflected wave is longer, it is more strongly attenuated than the incident wave leading to the mean setup of sea level. The magnitude of the setup depends on the ratio of the channel length and the wavelength of the tidal forcing. For a channel of 5–150 km length with depth varying laterally between 5 and 10 m, the setup can reach up to 12 cm given semi-diurnal forcing.

The quadratic bottom friction term in Equation 1 can also generate variability locally at the frequencies of even and odd harmonics of the incoming tidal wave (e.g., Parker, 1991). This tidal flow along a narrow channel is another example of the link between the mean state and overtides and will be important in explaining the distribution of predicted MDT near the head of the upper Bay of Fundy.

3. Ocean Models

Two models are used in this study. The three-dimensional, fully nonlinear, baroclinic ocean model of the Gulf of Maine and Scotian Shelf (GoMSS) was developed by Katavouta and Thompson (2016). A higher resolution barotropic model of the upper Bay of Fundy, within the model domain of GoMSS, was developed specifically for this study. This new model will henceforth be referred to as UBoF. The domains of both models are shown in Figure 1. Further details are given below.

3.1. Gulf of Maine and Scotian Shelf

For the present study, the GoMSS model was upgraded to version 3.6 of the Nucleus for European Modeling of the Ocean (NEMO; Madec et al., 2017). The x-axis of the coordinate system is aligned with the large-scale orientation of the coastline with an anti-clockwise rotation of 23.6° relative to geographic coordinates (E-W, S-N). The horizontal grid spacing is 1/36° which corresponds to 2.1–2.5 km in the x-direction and 2.9–3.6 km in the y-direction.

In the vertical, the model grid consists of 52 levels which, in a state of rest, increase in spacing from 0.72 m at the surface to 235.33 m at the bottom. The maximum depth of the bathymetry is clipped at 4,000 m. GoMSS uses the z*-coordinate approach (Levier et al., 2007) which allows for large variations of the (nonlinear) free surface. In this variable volume formulation the level spacing varies over time with sea surface height. At the bottom, partial cells are used to better resolve the bathymetry.

The TKE turbulent closure scheme used in the original configuration of GoMSS was replaced by the k-ϵ-closure scheme (Rodi, 1987) using the Generic Length Scale (GLS) formulation (Umlauf & Burchard, 2003, 2005). The enhanced vertical diffusion of momentum applied in the original configuration was turned off. Furthermore, an iso-level Laplacian diffusion operator is used instead of a biharmonic operator for stability reasons. The background lateral eddy viscosity coefficient A_h^m was taken to be 50 $m^2 s^{-1}$ (Table 1).

A nonlinear parameterization of bottom friction, with enhancement in the logarithmic boundary layer, is used. This means the drag coefficient c_d is dependent on the thickness of the model grid cell above the bottom. The minimum value of c_d was set to 2.50×10^{-3} (Table 1). At the coast, a partial slip boundary condition with a slip parameter of 0.5 is applied (see Madec et al., 2017, for details).

GoMSS was initialized on 1 January 2010 and run for 3 months. For the initial and lateral boundary conditions, temperature, salinity, sea surface height, and currents were taken from the HYCOM-NCODA system (Chassignet et al., 2007). The boundary forcing was supplemented with tidal elevations and currents computed using five constituents (M_2, N_2, S_2, k_1, O_1) from FES2004 (Lyard et al., 2006). Surface forcing at the air-sea interface was taken from the Climate Forecast System Reanalysis (Saha et al., 2010). The air-sea fluxes of heat and momentum for GoMSS were calculated using the bulk formulae of Large and Yeager (2004) and data for the following variables: wind at 10 m; air temperature and specific humidity at 2 m; precipitation rate; longwave and incoming short wave radiation.

Given GoMSS is initialized with realistic, three-dimensional hydrographic information, the spin-up of the model depends primarily on the tides. Based on visual inspection of the time series of model output from multiple runs, the spin-up time is estimated to be about 2 days. The tidal amplitudes and phases presented below are estimated from the last month of the 3 month simulation.

Table 1
Overview of Model Runs

Run	Model	Bathymetry	A_h^m [$m^2 s^{-1}$]	c_d [$\times 10^{-3}$]
GoMSS	GoMSS	ETOPO2v2*	50	2.5
CTRL	UBoF	GEBCO & Observations	20	4.0
B1	UBoF	GoMSS, nearest neighbor	20	4.0
B2	UBoF	GoMSS, linear interpolation	20	4.0
B3	UBoF	GoMSS, cubic interpolation	20	4.0
S	UBoF	GEBCO & Observations	10, 20, …, 50	2.5, 3.0, …, 4.5

Note. GoMSS (1/36° grid spacing) is the Gulf of Maine and Scotian Shelf regional ocean model. CTRL is the control run of the barotropic high-resolution ocean model UBoF (1/144° grid spacing) covering the upper Bay of Fundy (see Figure 1). Runs B1-B3 use the same high-resolution grid and model parameters as CTRL, but the bathymetry is replaced by the GoMSS bathymetry estimated using three interpolation schemes. The "S" runs explore the effect of varying the background lateral eddy viscosity coefficient A_h^m and minimum bottom friction coefficient c_d (refer to Section 3.2 UBoF). A_h^m was varied from 10 to 50$m^2 s^{-1}$ by increments of 10$m^2 s^{-1}$. Similarly, c_d was varied from 2.5×10^{-3} to 4.5×10^{-3} by increments of 0.5×10^{-3}. This is indicated by the "…" in the parameter ranges of the "S" runs. All model runs are for three months starting 1 January, 2010.

*Higher-resolution data were used to improve the bathymetry in the inner Gulf of Maine (see Katavouta & Thompson, 2016, for details).

3.2. Upper Bay of Fundy

The strong tidal flow in the Bay of Fundy mixes the water column and therefore vertical stratification is negligible (Tee, 1977). For this reason, UBoF is a barotropic model with constant temperature and salinity forced only by tides along its open boundary. UBoF is based on the same version of NEMO as GoMSS, but only covers the upper Bay of Fundy (Figure 1b). In comparison to GoMSS, the UBoF horizontal grid is refined by a factor of 4 resulting in an average grid spacing of 555 m in the along domain direction (aligned with the x-axis of GoMSS) and 785 m in the cross-domain direction. The vertical grid, turbulence closure schemes, and the formulation of the lateral diffusion operator, are the same as in GoMSS. Although the model grid is three-dimensional, the underlying dynamics are well represented by the depth-averaged Equations 1 and 2.

The bathymetry for UBoF was created by combining the 30′′ General Bathymetric Chart of the Oceans (GEBCO, Weatherall et al., 2015) with more than 1,22,000 in-situ measurements using optimal interpolation. Note that NEMO version 3.6 does not allow for wetting and drying of model grid cells and therefore, a minimum water depth (H_{min}) has to be specified. We use the approach of Maraldi et al. (2013) to deal with locations where the maximum tidal amplitude exceeds $H_{min} = 5$ m.

The prediction of tides by non-global ocean models is strongly dependent on the quality of the open boundary conditions. UBoF was forced with tidal elevation and currents for five semi-diurnal and diurnal constituents (M_2, S_2, N_2, K_1, O_1) obtained from the Scotia-Fundy-Maine Data of WebTide (Dupont et al., 2005). WebTide is a tidal prediction model that assimilates tidal amplitudes and phases estimated from satellite altimetry data at crossover points. This modeling tool is based on a finite element forward model and linear harmonic inverse model that is used to assimilate both satellite altimetry and coastal sea level observations by tide gauges. The predicted tidal elevations and currents have been shown to be in excellent agreement with observations (see Dupont et al., 2002, 2005, for details). We will also assess the predictions for our study region, and the specific WebTide dataset used here, in the following section.

The control run of UBoF (henceforth CTRL, Table 1) was chosen based on the validation of multiple runs. Runs B1-B3 use the same high-resolution grid and model parameters as CTRL, but the bathymetry has been replaced by the GoMSS bathymetry interpolated to the UBoF grid. Downscaling the GoMSS model bathymetry to the UBoF grid can be done in multiple ways. We tested three well-known schemes, including "nearest neighbor" interpolation which can generate strong gradients in the gridded bathymetry that we thought may generate significant nonlinear effects. The "S" runs explore the effect of varying the background lateral eddy viscosity coefficient A_h^m and minimum bottom friction coefficient c_d using ranges of parameter values that are typical for high-resolution ocean models ("S" stands for sensitivity).

The amplitude and phase of the predicted tidal elevation were calculated using tidal analysis routines that are part of the NEMO code. Ellipse parameters of the tidal currents were estimated offline from the hourly predictions of depth-averaged currents using a simple (no inference) least squares method with a Rayleigh coefficient of $R = 0.95$. (This coefficient is used in the Rayleigh selection criterion which requires $|\omega_1 - \omega_2|T_r > R$ where T_r is the minimum record length needed to statistically separate two tidal constituents with frequencies ω_1 and ω_2 in cycles per unit time. For more details, see Foreman and Henry (1989)). Prior to tidal analysis, the predicted horizontal current components, which are defined on the Arakawa C-grid of the model, were linearly interpolated to the center of each grid cell. The current vectors were then rotated from the grid coordinates to geographic coordinates. Predicted tidal ellipse parameters and mean currents were then estimated from the time series at the center model grid points closest to the ADCP locations in Figure 1.

4. Observations

Tidal amplitudes and phases, estimated from sea level records from 14 coastal tide gauges, were provided by the Canadian Hydrographic Service (CHS, S. Nudds, 2017; personal communication). Additional observations made by three bottom pressure gauges were made available by Dr. D. Greenberg (Bedford Institute of Oceanography, BIO, 2018; personal communication). Figure 1b shows the locations of all 17 observation sites (More information about the observed records can be found in S1).

The number of constituents resolved by the tidal analyses depends on record length. This ranges from 21 to 197 days across the 17 locations. It was possible to resolve M_2, S_2, n_2, K_1, O_1, and M_4 at all sites, except for N_2 at Spencers Island (station 242). The longest available sea level record (168 days) was for Cape D'Or (station 240). It was obtained from the Marine Environmental Data Section (MEDS) of the Department of Fisheries and Oceans Canada. To quantify the uncertainty of the amplitudes and phases estimated from the shorter records, the 168-day record from Cape D'Or was split into non-overlapping 29-day blocks and a tidal analysis was performed on each block. The standard deviation of the estimated amplitudes and phases was then used to obtain approximate 95% confidence intervals for 29-day records. The halfwidth of the confidence intervals was found to be 0.09 m for all of the semi-diurnal amplitudes and 1°, 5° and 7° for the phases of M_2, N_2, and S_2, respectively. These values are similar to the estimates made by Dupont et al. (2005) based on an analysis of an 89-day observed record from Minas Basin. For the diurnal and M_4 tides, the halfwidths of the 95% confidence intervals are $\mathcal{O}(1\text{ mm})$ for the amplitudes and 1°, 2°, and 2° for the phases of K_1, O_1, and M_4, respectively.

Observed tidal ellipse parameters and the time mean of depth-averaged currents, both obtained from Wu et al. (2011), are also used to validate the model predictions. These estimates are based on observations made by bottom-mounted Acoustic Doppler Current Profilers (ADCPs) deployed at 10 stations in Minas Passage and Minas Basin (see Figure 1c for locations). The lengths of the ADCP records range between 21 and 41 days. For additional details of the ADCP observations, and the data processing, see Wu et al. (2011).

5. Validation of Tides and Mean Current

We first validate the control run of UBoF (CTRL, Table 1) for M_2 elevation and currents. Next, we validate M_4 elevation and currents, and finally the mean currents. This is the first time that a tidal model of the upper Bay of Fundy has been validated using observed values of M_4 tidal elevation. The MDT, for which no reliable observations exist, is discussed in the following section.

In addition to the root mean squared error (RMSE), the following metric is used to validate the predicted tides at N stations:

$$\tilde{\gamma}^2 = \frac{\sum_{i=1}^{N} \int_0^T |\tilde{\mathbf{x}}_{o,i}(t) - \tilde{\mathbf{x}}_{m,i}(t)|^2 \, dt}{\sum_{i=1}^{N} \int_0^T |\tilde{\mathbf{x}}_{o,i}(t)|^2 \, dt}. \quad (7)$$

Here, $\tilde{\mathbf{x}}_{o,i}$ and $\tilde{\mathbf{x}}_{m,i}$ are the observed and predicted tidal variables, respectively, for station i. Each variable is expressed as a sinusoidal function of time t with frequency $\omega = 2\pi/T$, where T is the tidal period. The $\tilde{\gamma}^2$ metric can be used to assess the fit of either tidal elevations or currents. For the latter it takes into account errors in

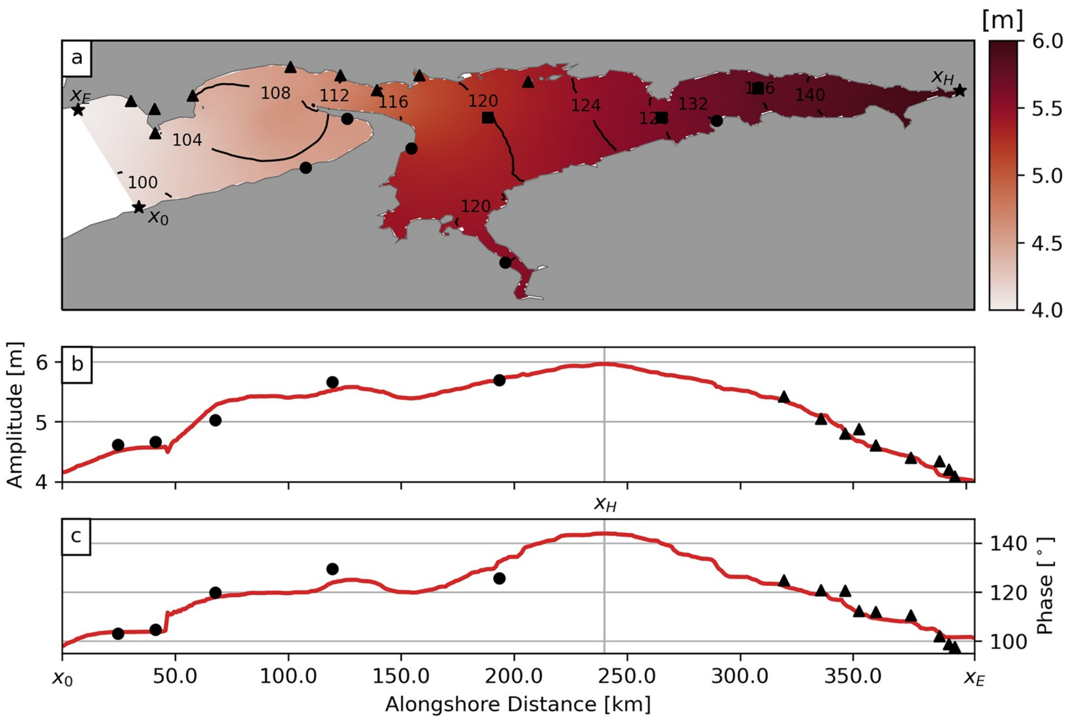

Figure 2. Predicted and observed amplitude and phase of M_2 tidal elevation. (a) Colors show the tidal amplitude in meters and contours show phase in degrees relative to Greenwich predicted by CTRL. Circles and triangles mark the tide gauges along the southern and northern coast, respectively. Squares indicate offshore locations. Black stars mark alongshore reference points. Panels (b) and (c) show observed (black symbols) and predicted (red lines) coastal M_2 tidal amplitude and phase as a function of distance along the coast measured counterclockwise from x_0 on the open boundary, to the head of the basin at x_H, and back to x_E on the open boundary along the north shore.

the principal axes of tidal current and also phase. This metric is based on Katavouta et al. (2016) but has been extended to summarize the fit for multiple stations.

The mean currents are validated in a similar way:

$$\overline{\gamma}^2 = \frac{\sum_{i=1}^{N} \left|\overline{\mathbf{u}}_{o,i} - \overline{\mathbf{u}}_{m,i}\right|^2}{\sum_{i=1}^{N} \left|\overline{\mathbf{u}}_{o,i}\right|^2}, \tag{8}$$

Where $\overline{\mathbf{u}}_{o,i}$ and $\overline{\mathbf{u}}_{m,i}$ are the observed and predicted mean currents at observation location i. The bar indicates a time mean.

For both metrics, the smaller γ^2 the better the fit of the model to the observations in terms of error variance. More specifically, if $\gamma^2 < 1$ the error variance is less than the variance of the observations and, in this sense, the model has some skill. If $\gamma^2 = 0$, the model fits the observations perfectly. If $\gamma^2 > 1$, the model has no skill (the error variance exceeds the variance of the observations). Both metrics can be used to assess fit at one or more ($N > 1$) stations.

5.1. M_2 Elevations and Currents

The amplitude and phase of the M_2 tidal elevations predicted by CTRL are shown in Figure 2. Panel (a) shows the predicted amplitude and phase across the whole model domain and panels (b) and (c) show the amplitude and phase along the coast. The x-axis in these two panels is alongshore distance measured counterclockwise from x_0 on the open boundary, to the head at x_H, and then along the north shore to x_E where the coastline intersects the open boundary. The black circles in all three panels show the locations of coastal tides gauges along the south shore. The black triangles are for locations along the north shore.

Table 2
Summary of Fit of Model Predictions to Sea Level and Current Observations Using the γ^2 Metric

Variable	Constituent	CTRL	"S" runs	GoMSS	WebTide
η	M_2	0.005	0.005–0.007	0.018	0.006
η	S_2	0.022	0.021–0.024	0.325	0.022
η	N_2	0.050	0.047–0.055	0.079	0.042
η	M_4	5.577	5.089–6.072	16.887	1.841
u	M_2	0.023	0.022–0.027	0.201	0.034
u	M_4	0.329	0.325–0.393	1.924	0.325
u	Mean	0.303	0.264–0.410	0.876	-

Note. Predicted sea level (η) and depth mean current (**u**) have been validated against observations at several tidal frequencies and the mean. The UBoF runs (CTRL and "S" runs) are defined in Table 1. The same metrics are given for GoMSS and WebTide (last two columns). The same observations from 14 coastal tide gauges, 3 bottom pressure gauges, and 10 ADCPs were used for all models. The γ^2 metrics are defined by Equations 7 and 8.

Along the open boundary (clockwise from x_0 to x_E), the predicted mean M_2 amplitude is 4.07 m and it increases to 5.96 m at the head of Cobequid Bay (x_H). The tidal phase also increases toward the head with high water arriving at x_H with a delay of about 1.5 hr relative to the open boundary. The predicted increase in M_2 amplitude and phase toward the head is consistent with previous studies (e.g., Greenberg, 1969; Hasegawa et al., 2011; Karsten et al., 2008; Tee, 1976; Wu et al., 2011) and has been explained in terms of the resonant character of the Bay of Fundy system (Garrett, 1972).

The agreement between the observed and predicted M_2 elevation at the 14 coastal tide gauges is shown by the black dots and triangles along the south shore and north shore, respectively, in Figures 2b and 2c. The RMSEs in amplitude and phase for the CTRL run are 0.12 m and 3.4°, respectively, and $\tilde{\gamma}^2 = 0.005$. Using observations from all 14 coastal tide gauges, and the three additional pressure gauges shown by the black squares in Figure 2a, the RMSEs are 0.17 m and 3.5° for amplitude and phase, respectively, and $\tilde{\gamma}^2 = 0.005$. These error metrics are similar to those of WebTide based on the same observations (RMSEs for amplitude and phase are 0.13 m and 4.03°, respectively; $\tilde{\gamma}^2 = 0.006$, see Table 2). This is not surprising because UBoF is forced with tidal elevations taken from WebTide (see Section 3).

Next, the fit of the model to the observed, depth-mean M_2 tidal currents at the 10 ADCP locations is examined (Figure 1c). The M_2 tidal ellipses are shown in Figure 3. The dots correspond to the position of the tidal current at the time of the maximum equilibrium tide at the Greenwich meridian. Strong, rectilinear M_2 tidal currents are evident in Minas Passage (locations A1-A4, A8, and S1-S3) with speeds exceeding 3 $\mathrm{m\,s^{-1}}$. Inside Minas Basin (A5 and A6), the currents are weaker with maximum M_2 speeds of about 1 $\mathrm{m\,s^{-1}}$. Based on visual comparison, the predictions are in good agreement with the observations and this is confirmed by the low values of $\tilde{\gamma}^2$ for each location given in the lower left corner of each panel. Combining results for all ADCP locations, $\tilde{\gamma}^2 = 0.023$. This is a slight improvement over WebTide ($\tilde{\gamma}^2 = 0.034$) and a significant improvement over GoMSS ($\tilde{\gamma}^2 = 0.201$, see Table 2).

As a further check on the model, predictions of tidal elevation for S_2 and N_2 were also compared to observations. The $\tilde{\gamma}^2$ values (Table 2) show the performance of CTRL is comparable to WebTide, and slightly better than GoMSS.

Summarizing the results of this subsection, UBoF provides good predictions of M_2 tidal elevations and currents in the study region.

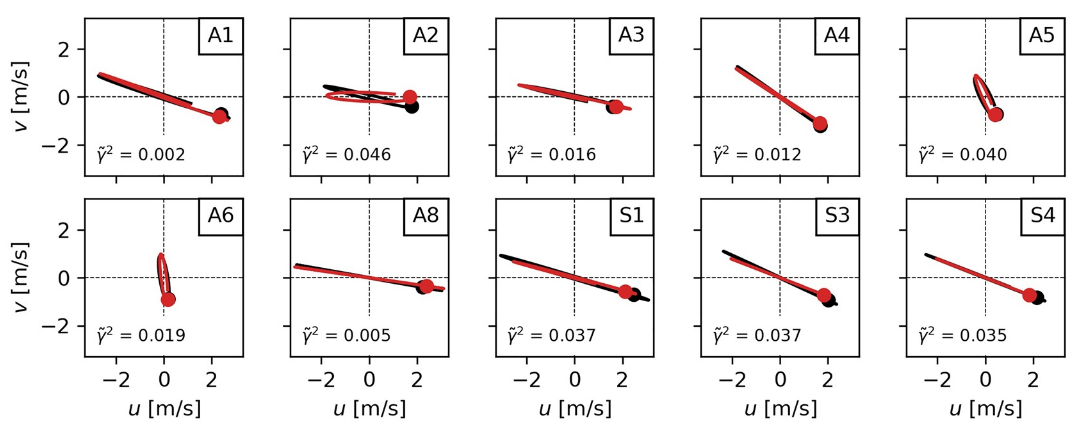

Figure 3. M_2 tidal ellipses of depth-averaged current at the 10 Acoustic Doppler Current Profiler locations shown in Figure 1c. The ellipses for observations and CTRL predictions are shown in black and red, respectively. The last tenth of the tidal cycle is omitted to indicate the sense of rotation. The dot shows the initial time. $\tilde{\gamma}^2$ for each station is given in the lower left corner of each panel. The speeds are in m s $^{-1}$.

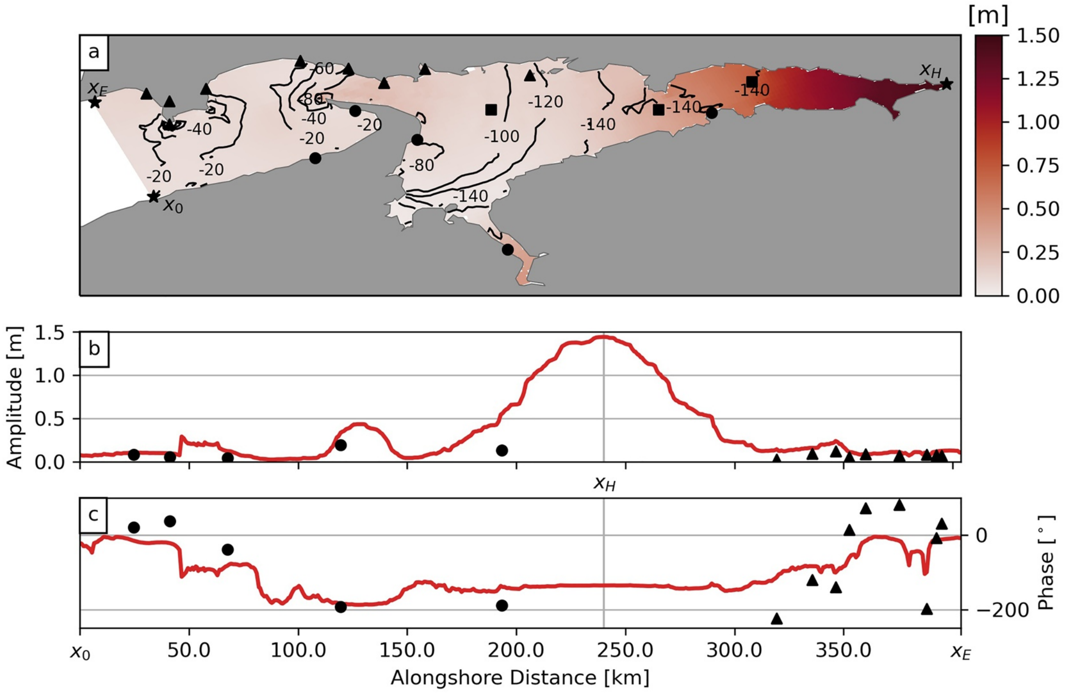

Figure 4. Predicted and observed amplitude and phase of M_4 tidal elevation. (a) Colors show the tidal amplitude in meters and contours show phase in degrees relative to Greenwich predicted by CTRL. Circles and triangles mark the tide gauges along the southern and northern coast, respectively. Squares indicate offshore locations. Black stars mark alongshore reference points. Panels (b) and (c) show observed (black symbols) and predicted (red lines) coastal M_4 tidal amplitude and phase as a function of distance along the coast measured counterclockwise from x_0 on the open boundary, to the head of the basin at x_H, and back to x_E on the open boundary along the north shore.

5.2. M_4 Elevation

The M_4 amplitude and phase of elevation predicted by CTRL are shown in Figure 4. The largest amplitudes are predicted for Cobequid Bay reaching 1.44 m at the head (x_H). Unfortunately, no observations are available for this region. In the Avalon River (Figure 1b), M_4 amplitudes reach 0.43 m. At Cape Split and in Minas Passage, CTRL predicts amplitudes of 0.41 and 0.26 m, respectively. These local maxima can be explained by the Bernoulli effect as well as vorticity generation and subsequent advection due to the strong tidal currrents through the narrow strait (see Section 2.1).

The phase mapped in Figure 4a suggests M_4 in the upper reaches of Cobequid Bay is standing. This is indicated by the approximately constant tidal phase of about $-140°$ in this region (see Figure 4c for alongshore distances of 170–290 km). Beyond these regions, the phase suggests propagation as a shallow water wave toward the open boundary.

The alongshore variation of observed and predicted M_4 tidal elevation at the coast is shown in Figures 4b and 4c. It is clear that the overall agreement at the 14 coastal tide gauges is poor, for example, the predicted amplitudes are generally too large, and the phase changes in the vicinity of Minas Passage are too small. This poor agreement is confirmed by large RMSEs of 0.12 m and 65.1° for M_4 amplitude and phase and $\tilde{\gamma}^2 = 3.3$. Adding observations from the three bottom pressure gauges (squares in Figure 4a) gives combined RMSEs for amplitude and phase of 0.19 m and 62.6° and $\tilde{\gamma}^2 = 5.6$. Clearly, CTRL has no skill in predicting M_4 elevation at the coast (Table 2). WebTide also performs poorly with RMSEs for amplitude and phase of 0.10 m and 74.6° and $\tilde{\gamma}^2 = 1.8$ (Table 2).

The M_2 and M_4 amplitude and phase at the three offshore bottom pressure locations (squares in Figures 1b and Table 3) are now examined. At the most western gauge in Minas Basin (40258), the predicted M_4 amplitude is 0.12 m which corresponds to an M_4/M_2 amplitude ratio of 0.022. The observed M_4 amplitude at this location is 0.01 m and the observed M_4/M_2 amplitude ratio is only 0.002. Moving toward the head of the basin, both the model and observations show an increase in M_4, however, the predicted amplitude at the eastern most gauge in

Table 3
Observed and Predicted Amplitude and Phase for M_4 Elevation at the Three Bottom Pressure Gauges (Squares in Figure 1b)

Station		M_4 Amp. [m]	M_4 Phase [°]	M_4/M_2	$2\theta_{M_2} - \theta_{M_4}$ [°]
40258	Observations	0.01	−55.1	0.002	296.8
	UBoF CTRL	0.12	−94.0	0.022	333.3
	WebTide	0.12	−134.1	0.023	23.1
40262	Observations	0.09	162.0	0.016	88.9
	UBoF CTRL	0.35	−144.6	0.063	41.5
	WebTide	0.25	−156.6	0.044	56.7
40264	Observations	0.18	164.6	0.029	94.1
	UBoF CTRL	0.72	−141.1	0.125	52.6
	WebTide	0.41	−157.9	0.069	67.9

Note. M_4/M_2 is the amplitude ratio and $2\theta M_2$ - θM_4 is the phase of M_4 relative to M_2 at the same location. The row order of the stations is from west to east.

Cobequid Bay (40264) is four times larger than observed (Table 3). This discrepancy is also reflected in the observed and predicted M_4/M_2 ratios at that station.

The observed and predicted M_4 phases at the three bottom pressure locations are listed in Table 3. At the two eastern locations (stations 40262 and 40264), the observed M_4 phases agree within about three degrees (162.0° and 164.6°), consistent with a standing oscillation in Cobequid Bay (see also Figure 4a). The phase at the western station (40,258) is −55.1°, consistent with westward propagation from this region. The M_4 phases predicted by UBoF exhibit similar behavior: the phases at the two eastern stations are within 4° (−144.6° and −141.1°) and the phase at the western location (−94.1°) suggests propagation away from Cobequid Bay. Differences exist however in the M_4 phase relative to the M_2 tide. At the two eastern bottom pressure gauges, the observed relative phase $2\theta_{M_2} - \theta_{M_4} \approx 90°$ which indicates flood dominance with maximum asymmetry between a short flood period with strong currents and longer ebb duration with weaker currents (Friedrichs & Aubrey, 1988). This flood dominance is also predicted by CTRL, however, the tidal distortion is less pronounced than the observations ($2\theta_{M_2} - \theta_{M_4} = 52.6°$ for the eastern station in Cobequid Bay, 40264). The presence of tidal flats, which are prevalent in this region, can have a significant influence on the distortion of the tidal wave (e.g., Speer & Aubrey, 1985). This is not captured in UBoF because it does not include wetting and drying.

The above discussion leads us to speculate that the M_4 tide predicted by UBoF is contaminated by an unrealistically large signal that is generated in Cobequid Bay and subsequently propagates westward toward the open boundary. To test this speculation, the predictions of M_4 tidal elevation at all 11 tide gauges to the west of bottom pressure gauge 40258 (henceforth the reference station) were corrected as follows:

$$A'_j = A_j - A_{\mathrm{ref}} exp\left[i\Delta\theta\left(\frac{\lambda_j - \lambda_{\mathrm{ref}}}{\lambda_0 - \lambda_{\mathrm{ref}}}\right)\right], \qquad \text{with } j = 1, \ldots, 11 \tag{9}$$

Where A_j is the complex M_4 amplitude at the jth tide gauge and A_{ref} is the complex M_4 amplitude at the reference station. λ_j, λ_{ref} and λ_0 are the longitudes of the jth tide gauge, the reference station, and the most western tide gauge (235), respectively. The only free parameter in Equation 9 is $\Delta\theta$, the spatial change in phase associated with a shallow water wave propagating at constant speed from the reference station to the open boundary. The optimal value was determined by minimizing $\tilde{\gamma}^2$ and corresponded to a time lag of 1.0 hr, implying a phase speed of 13 m s^{-1}.

Table 4
$\tilde{\gamma}^2$ for Original and Corrected Predictions of M_4 Elevation at Coastal Tide Gauges (see Figure 1b)

Station	CTRL	CTRL corr.	WebTide	WebTide corr.
235	1.484	0.161	0.177	2.584
236	0.328	1.082	0.499	5.070
240	2.224	0.151	1.370	0.935
242	3.953	0.180	1.754	0.191
245	1.892	0.019	0.677	0.329
247	4.143	0.472	7.159	1.010
250	1.829	0.202	1.343	0.371
255	1.285	0.484	0.581	0.389
290	4.475	0.891	8.683	2.241
300	2.204	0.461	1.241	1.340
305	0.569	0.358	0.810	1.062

Note. The corrections were made using Equation 9. All stations are west of the reference bottom pressure gauge 40258. See Section 5.2 for details.

The "station referencing" technique based on Equation 9 was used to adjust the observed and predicted M_4 amplitudes. This allows us to assess how well the local generation of overtides is captured by the model. The resulting $\tilde{\gamma}^2$ are listed in Table 4. The correction significantly improves the model fit of CTRL at all but one station and thus supports the speculation that the large M_4 error is generated remotely in Cobequid Bay. This example clearly highlights a potential problem with using M_4 elevation for model validation; the fit at a given location can be dominated by remotely generated errors. The spatial referencing technique outlined above is one way of overcoming this limitation and extracting useful information from M_4 elevations for validation.

5.3. M_4 Currents

The M_4 tidal ellipses calculated from observed and predicted depth-averaged currents are shown in Figure 5. The $\tilde{\gamma}^2$ values are given in the lower left corner of each panel. Both observations and predictions agree that the

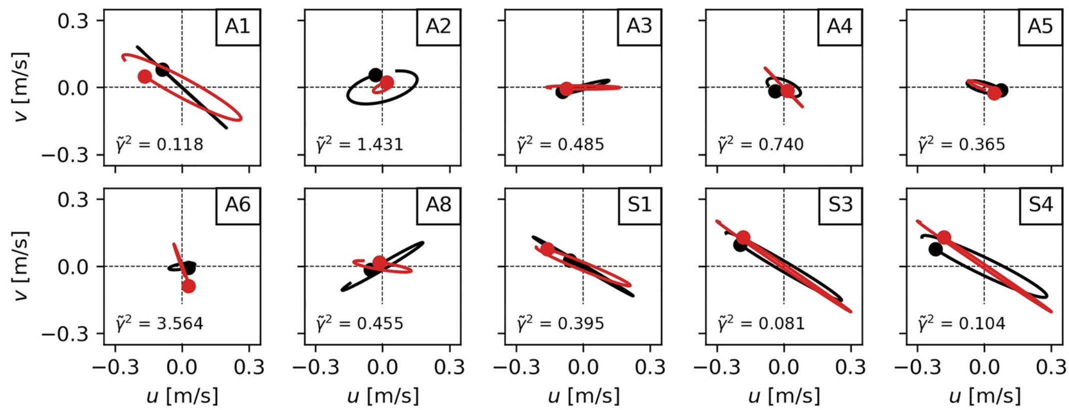

Figure 5. Predicted (red) and observed (black) M_4 tidal ellipses of depth-averaged currents. The format is the same as in Figure 3.

strongest M_4 currents occur in Minas Passage (A1-A4, A8, and S1-S3) where speeds approach 0.3 $\mathrm{m\,s^{-1}}$. Inside Minas Basin (A5 and A6), the currents are much weaker and $\mathcal{O}(0.1\ \mathrm{m\,s^{-1}})$.

Generally, locations with strong observed M_4 currents also have strong M_4 predictions. The only exception is A2. The individual values of $\tilde{\gamma}^2$ show the model has skill in predicting M_4 currents at most locations. For all ADCP stations combined, $\tilde{\gamma}^2 = 0.329$ which is comparable to WebTide ($\tilde{\gamma}^2 = 0.325$, see Table 2). These values of $\tilde{\gamma}^2$ indicate better prediction of M_4 current than M_4 tidal elevation.

As discussed in Section 2, both nonlinear advection and bottom friction can generate overtides. As a result, strong M_4 currents are often observed around headlands (Geyer & Signell, 1990) and in regions where strong M_2 currents vary on small spatial scales (Davies & Lawrence, 1994). In the previous section, it was shown that the strongest M_2 currents are observed (and predicted) in Minas Passage. This results in flow separation at Cape Split and Cape Blomidon, an asymmetry in the flow pattern between flood and ebb (Tee, 1976), and strong M_4 currents on either side of these two promontories (Geyer & Signell, 1990; Mardell & Pingree, 1981).

There is no obvious relationship between the orientation of the M_4 and M_2 currents (cf. Figures 3 and 5). However, it will be shown in the next section that both the predicted and observed M_4 currents are closely aligned with the mean circulation. This is in agreement with the figures presented by Hasegawa et al. (2011).

5.4. Mean Currents

The streamlines of the predicted depth-mean currents averaged over the 3-month model simulation, are shown in Figure 6a. The mean circulation is strongest in and around Minas Passage where four permanent eddies can be seen (I-IV). Overall, this circulation is in qualitative agreement with previous studies (e.g., Greenberg, 1983; Hasegawa et al., 2011; Tee, 1976, 1977; Wu et al., 2011). The four permanent eddies have already been identified and explained by Tee (1976) based on vorticity arguments, idealized model simulations, and model runs with more realistic bathymetry and coastline. He showed that the eddies are due to the combined effect of vorticity generation close to shore, subsequent advection by the tidal flow and non-local dissipation (see Section 2.1).

Figure 7 is an enlarged view of the mean flow in Minas Passage with the predicted mean flow shown as gray vectors at every model grid point. Black vectors show the time mean of the observed depth-averaged currents calculated at the 10 ADCP stations. Overall, this circulation pattern is in agreement with the observations. The time-mean depth-averaged circulation predicted by CTRL is also consistent with additional observations made by current meters (Tee, 1977) which are not shown here.

To quantify the model fit, we calculated $\overline{\gamma}^2$ using the model predictions at the grid points closest to the observation locations. The resulting values are given in Table 5. There is general agreement between the observed and predicted mean currents at the 10 locations with the overall $\overline{\gamma}^2 = 0.303$. The reason for the large values of $\overline{\gamma}^2$ at some sites is a slight misplacement of the eddies in the model with respect to the observations (see Figure 7). It is

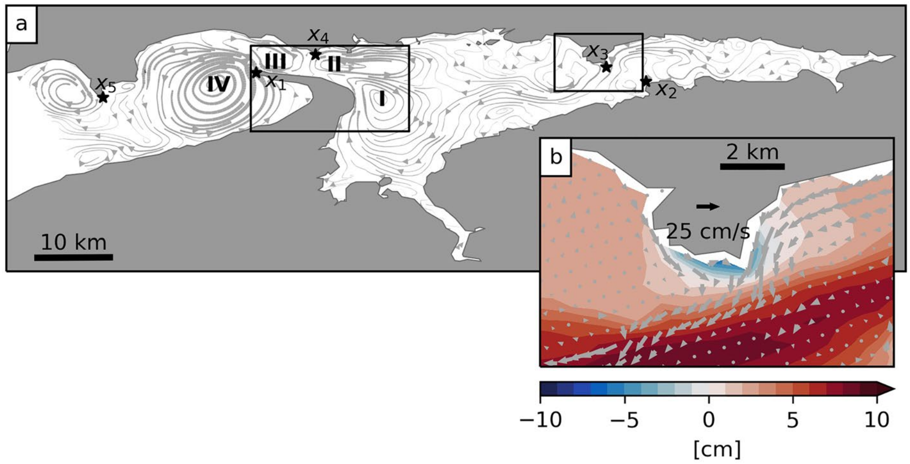

Figure 6. Predicted time mean of depth-averaged currents. (a) Streamlines predicted by CTRL. Stars mark alongshore points referenced in the text. (b) Predicted mean circulation around the headland at the alongshore reference point x_3. Colors show the predicted mean dynamic topography with the Bernoulli setdown removed.

important to note that for GoMSS the fit to the mean currents is significantly worse ($\overline{\gamma}^2 = 0.876$, Table 2). Mean currents from WebTide were not available.

In addition to the basin scale circulation, UBoF is also able to capture localized features that are generated by tidal flow around headlands. Figure 6b is a zoom of the predicted mean around the headland at x_3. On either side of the headland, a pair of counter-rotating eddies can be identified which join to form a strong mean offshore flow away from the tip. As discussed in Section 2.1, this is the result of vorticity generation caused by the tidal flow past the headland, followed by flow separation and non-local vorticity dissipation.

Overall, the above model validation shows that UBoF can predict the tides and mean currents in the upper Bay of Fundy including the nonlinear interactions that lead to overtides and the mean circulation. This increases our confidence in the predictions of MDT which will be discussed in the following section.

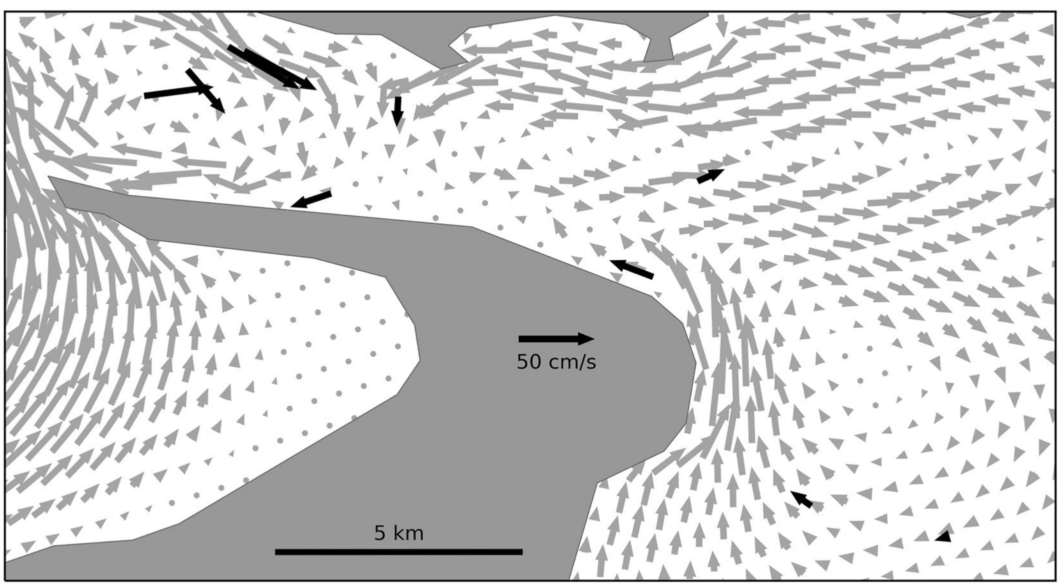

Figure 7. Time mean of depth-averaged currents around Cape Split. The black vectors show the observed values at the 10 Acoustic Doppler Current Profilers locations shown in Figure 1c. The gray vectors are the corresponding model predictions.

Table 5
$\overline{\gamma}^2$ for the Predicted Time Mean of Depth-Averaged Currents at Grid Points Closest to the 10 Acoustic Doppler Current Profilers Locations

A1	A2	A3	A4	A5	A6	A8	S1	S3	S4
0.000	0.577	0.080	0.210	0.017	0.101	0.972	0.426	0.058	0.061

6. Mean Dynamic Topography

In this section, we present the MDT in the upper Bay of Fundy predicted by CTRL and use the information about overtides to explain the differences in the MDT predictions by UBoF and GoMSS. The discussion focuses on the role of horizontal resolution and bathymetry which have the largest impact on the predicted MDT. We also assess the effect of changing model parameters related to bottom friction and horizontal mixing on the model predictions.

6.1. Prediction of MDT From UBoF

The MDT predicted by CTRL is shown in Figure 8. The dominant feature is the drop of almost 0.4 m in the Minas Passage which can be explained by the Bernoulli effect and the strong M_2 currents (see Section 2.1). This explanation is supported by the similar amplitude of M_4 elevation in this region (Figure 4b). More localized drops of MDT can also be seen around Cape Split and several headlands (e.g., x_3, x_4, and x_5). To quantify the MDT on the larger scale, we use the alongshore difference between locations A and B defined by $\Delta\overline{\eta} = \overline{\eta}_A - \overline{\eta}_B$. These locations were chosen to minimize the effect of local processes around headlands. From Figure 8 it is clear that the MDT inside Minas Basin is higher than in Minas Channel with $\Delta\overline{\eta} = 2.6$ cm.

The predicted MDT after correction for the Bernoulli effect is shown in Figure 9. This correction reduces the overall variability, but $\Delta\overline{\eta}$ remains positive (equal to 2.0 cm) and local depressions of MDT remain in the vicinity of Cape Split and the headlands mentioned above. At the head of Cobequid Bay a small setdown is predicted.

In order to explain this setdown, the Li and O'Donnell (2005) channel model (see Section 2.2) was extended to allow for forcing with multiple tidal constituents. If the tidal wave prescribed at the open boundary is the sum of a main tidal constituent and its first harmonic, for example, M_2 and M_4, the model can predict a setdown in mean sea level toward the end of the channel (not shown). This setdown can be explained in terms of the asymmetry in the forcing due to the inclusion of the overtide. More specifically, the predicted tidal wave entering Cobequid Bay

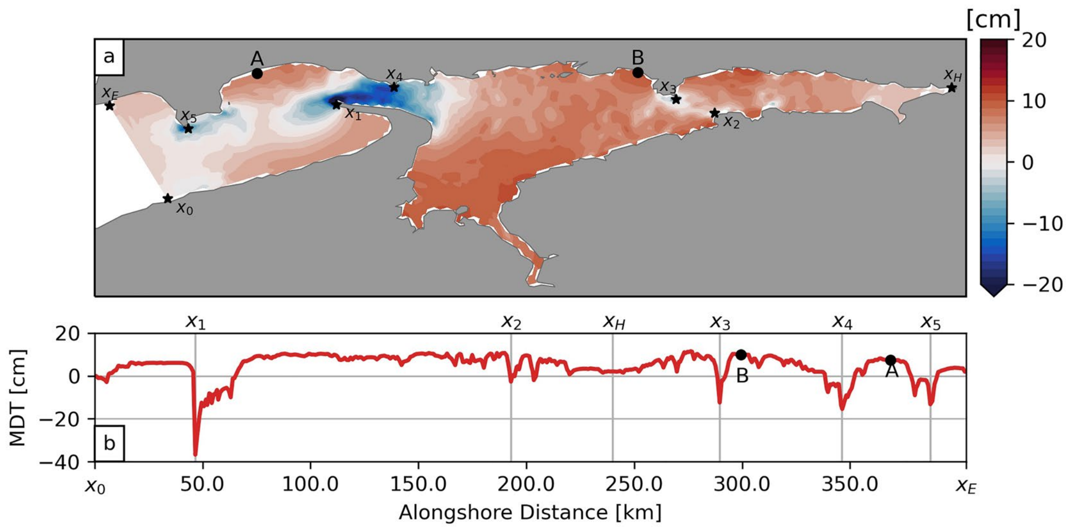

Figure 8. Mean dynamic topography (MDT) relative to the value at x_0 predicted by CTRL. (a) Model prediction of MDT. Note that the minimum at Cape Split (−37 cm) is outside the range of the colorbar. The two black dots A and B indicate the model grid points used to calculate $\Delta\overline{\eta}$. Stars mark alongshore reference points. (b) Predicted MDT as a function of alongshore distance from x_0.

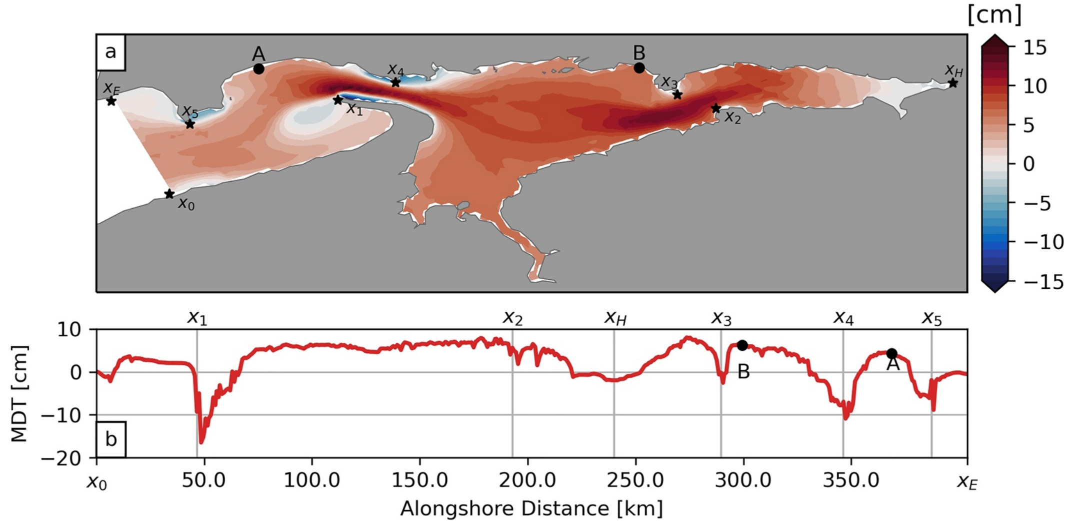

Figure 9. Mean dynamic topography prediction by CTRL with the mean Bernoulli setdown $-\overline{\mathbf{u}^2}/2g$ subtracted. The format is the same as in Figure 8.

has a significant M_4 amplitude (0.72 m at the western most bottom pressure gauge 40264, see Table 3) resulting in a strong and short inflow balanced by weaker and longer outflow. The net effect is a mean bottom stress that must be balanced by a pressure gradient leading to a setdown in mean sea level at the head (Pingree et al., 1984).

Figure 6b shows the Bernoulli-corrected MDT around the headland at x_3. A setdown at the tip of the headland is evident. As discussed in Section 2.1, tidal flow around a headland generates not only a mean Bernoulli setdown, but also a flow toward the tip. Along the coast, a pressure gradient is required to drive the mean flow toward the tip of the headland. An analysis of the predicted momentum balance shows that this pressure gradient is primarily balanced by bottom friction. Note that the setdown shown in Figure 6b is consistent with the "back-of-the-envelope" calculation in Section 2.1 that showed frictional and Bernoulli contributions to the setdown at the tip can be comparable. There is also a secondary contribution from the time mean of the $\zeta\hat{\mathbf{k}} \times \mathbf{u}$ term in the momentum equation, associated with the transient eddies generated either side of the headland. (The use of an Arakawa C-grid means the model sea level is not exactly at the coast where the $\zeta\hat{\mathbf{k}} \times \mathbf{u}$ term vanishes.) The same momentum balance holds for the predicted MDT setdowns at Cape Split (x_1) and in Minas Passage (x_4).

6.2. Using Observed Overtides to Identify Errors in Predicted MDT and Select the Optimal Model Bathymetry

We now explore the possibility of using overtides to assess the accuracy of MDT predictions. Particular attention is paid to the effect of spatial resolution and bathymetry, the most relevant differences between GoMSS and UBoF. As discussed in Section 5.2, neither model has skill in predicting M_4 elevation (Table 2) and therefore it has been excluded from the discussion below.

Figure 10 shows the joint variation of the alongshore tilt of MDT ($\Delta\overline{\eta}$, same scale for all panels) and γ^2 for different model runs. The MDT predicted by runs with poor fits ($\gamma^2 > 1$) to the observed overtides and mean currents will be considered unreliable.

GoMSS predicts a 6.1 cm setdown going into Minas Basin through Minas Passage. There is nothing in the fit of the observed and predicted M_2 elevations and currents that raises concern about the accuracy of this drop in mean sea level (Figures 10a and 10b). The corresponding plot for M_4 currents (Figure 10c) tells a different story: $\tilde{\gamma}^2$ is close to 2 indicating no predictive skill for the dominant overtide. Given the intrinsic relationship between MDT and overtides, this high value of γ^2 means that the GoMSS setdown must be considered suspect. This is further supported by the high value of $\overline{\gamma}^2$ for mean currents (Figure 10d).

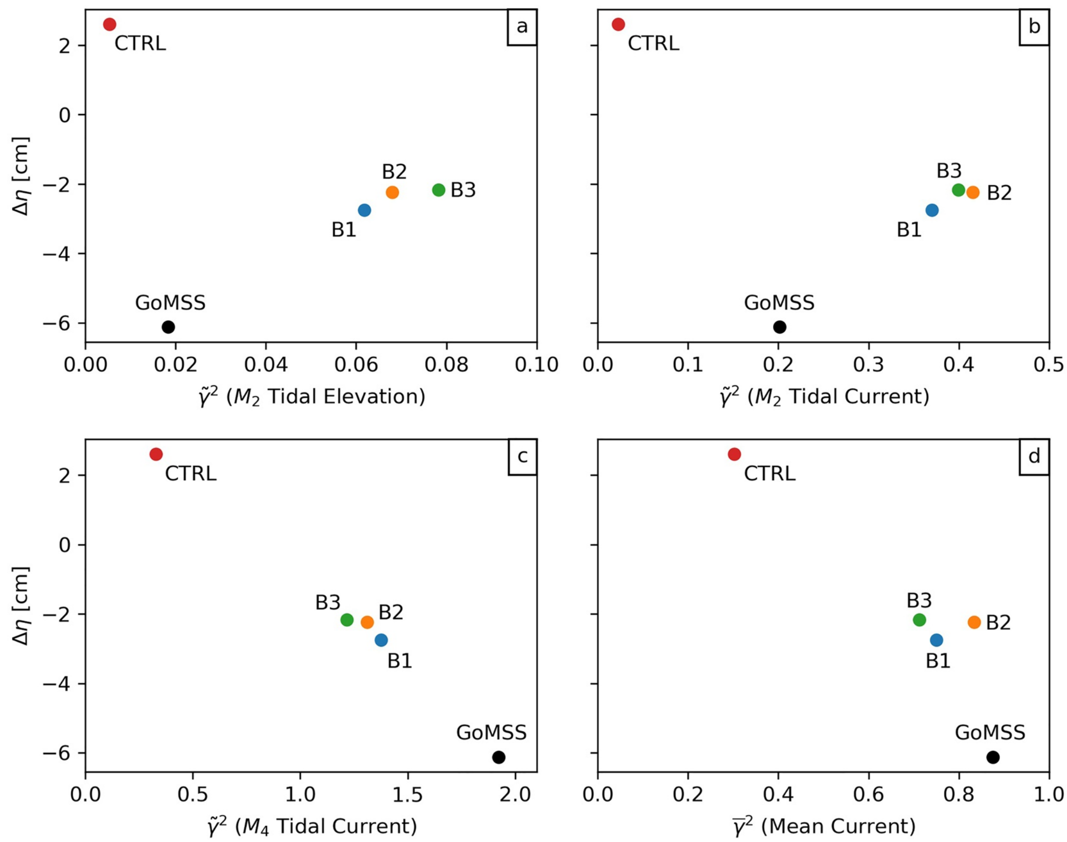

Figure 10. Mean dynamic topography difference $\Delta\overline{\eta}$ as a function of γ^2 for models with different horizontal resolution and bathymetry. The *x*-axis shows the following measures of model fit for (a) M_2 tidal elevation, (b) M_2 tidal current (c) M_4 tidal current and (d) mean current. Black dots show the results for Gulf of Maine/Scotian Shelf region (GoMSS). Runs B1-B3 use the same high-resolution grid, model parameters, and forcing as CTRL, but the bathymetry is replaced by the GoMSS bathymetry using different interpolation schemes (see Table 1 for details). Note the range of the *x*-axis varies among the panels.

The values of $\Delta\overline{\eta}$ and γ^2 for CTRL are also shown in Figure 10 (red dots). This run of UBoF predicts a 2.6 cm setup of mean sea level. The low values of γ^2 for M_4 and mean currents provide strong support in favor of the CTRL prediction of a small setup of MDT, and not the 6.1 cm setdown predicted by GoMSS.

Why does CTRL provide more accurate predictions of the overtides and mean currents at the ADCP locations? The CTRL configuration is superior to GoMSS in two respects: (a) its horizontal grid is refined by a factor of 4 compared to GoMSS, (b) its bathymetry has been generated specifically for UBoF (Section 3.2). The runs B1-B3 were designed to assess the effect of (b). They all have the same high-resolution grid and model parameters as CTRL, and differ only in the way the GoMSS bathymetry was interpolated to the UBoF grid (Section 3.2). The values of $\Delta\overline{\eta}$ and $\tilde{\gamma}^2$ for the runs B1-B3 are shown in Figure 10 (blue, orange and green dots).

In comparison to CTRL, the use of the interpolated GoMSS bathymetry in the runs B1-B3 degrades the model fit for all three interpolation schemes. In particular, for M_4 and mean currents, the values of γ^2 are close to 1. This demonstrates the added value of the in-situ depth measurements that were used to create the bathymetry of CTRL. Clearly, the realistic bathymetry in CTRL is critical for capturing the dominant nonlinear processes that generate overtides, and the mean state, in the upper Bay of Fundy. These results demonstrate how observed overtides can help select the optimal bathymetry of an ocean model in shallow, tidally dominated regions. They also highlight the additional information provided by overtides that cannot be obtained from the validation of astronomical constituents.

Relative to GoMSS, the interpolated bathymetry in runs B1-B3 degrades the fit for M_2 elevation and currents. Note that the bathymetry in GoMSS was optimized to accurately capture the tides in the whole Bay of Fundy

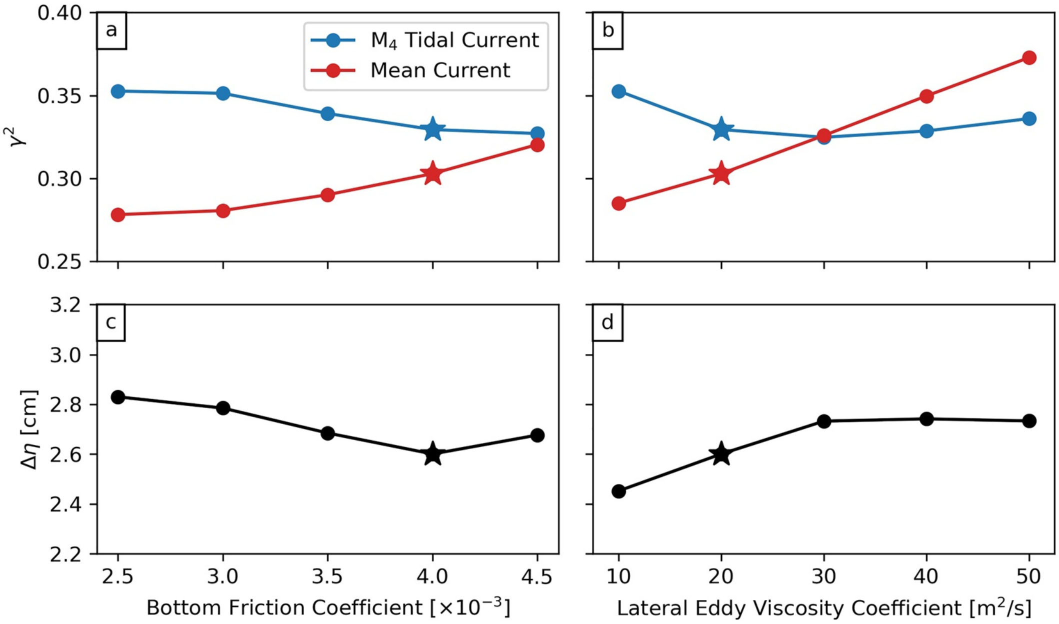

Figure 11. γ^2 and $\Delta\overline{\eta}$ as a function of bottom friction (a and c) and lateral eddy viscosity coefficient (b and d). The star indicates the UBoF control run (CTRL, see Table 1 for details).

using tidal forcing along the open boundaries of that model (Dr. A. Katavouta, 2021; personal communication). No such tuning was done for runs B1-B3. This is the likely explanation for the higher skill of GoMSS in predicting the M_2 tide compared to runs B1-B3. Despite a small improvement of model fit for M_4 and mean currents relative to GoMSS, the values of γ^2 are close to one indicating the B1-B3 runs are still unreliable.

The runs B1-B3 all predict $\Delta\overline{\eta}$ between −2 and −3 cm. This setdown is smaller than the GoMSS prediction, but still of opposite sign to the CTRL prediction. Based on the poor performance of runs B1-B3 in predicting overtides and the mean currents, these predicted setdowns have to be considered suspect.

Overall, the use of overtides leads to the conclusion that the large setdown in MDT predicted by GoMSS is highly suspect and the 2.6 cm setup predicted by the control run of UBoF is more realistic.

6.3. Sensitivity of γ^2 and $\Delta\overline{\eta}$ to Variations of c_d and A_h^m

Multiple runs of UBoF were performed to assess the impact of changing model parameters related to energy dissipation by bottom friction, horizontal and vertical mixing, and the formulation of the coastal boundary condition. The most important parameters were found to be the minimum bottom friction coefficient (c_d) and the background lateral eddy viscosity coefficient $\left(A_h^m\right)$.

The effect on model fit (γ^2) of systematically varying c_d and A_h^m over a realistic range, keeping all other model parameters fixed as in CTRL, is given by the "S" runs values in Table 2. Overall, the effect on tidal elevation and current at semi-diurnal frequencies is small. None of the "S" runs has useful predictive skill for sea level variations at the M_4 frequency $\left(\tilde{\gamma}^2 > 1\right)$ for the reasons given in Section 5.2. However, as detailed below, varying c_d and A_h^m does have a significant effect on M_4 tidal current and the mean current.

Figure 11 shows γ^2 (upper panels) and $\Delta\overline{\eta}$ (lower panels) as a function of c_d (left panels) and A_h^m (right panels). In all panels, the star shows the parameter value used in CTRL. Reducing c_d and A_h^m improves the fit to the observed mean current (red lines). The reason is that all of the UBoF runs generally underestimate the speed of the mean current (not shown) and reducing c_d and A_h^m leads to faster mean currents and a better fit to the observations. The effect of reducing c_d and A_h^m on the fit to M_4 tidal current (blue lines) is more subtle but it is clear that the worst fits are found for the smaller parameter values. This can be explained by an overestimation of the M_2 tidal currents and, as a result, an overestimation of the M_4 currents at low parameter values. These sensitivity studies show that it is not possible to clearly define a "best" set of model parameters. However, the use of observed overtides allows us to better constrain the parameter values, for example, we can rule out a bottom friction coefficient of 2.50×10^{-3} if the lateral viscosity coefficient is set to 20 $m^2 s^{-1}$.

The lower panels of Figure 11 show that the predicted large-scale MDT, as measured by $\Delta\overline{\eta}$, is insensitive to changes in c_d and A_h^m over realistic ranges with $2.4\ \text{cm} < \Delta\overline{\eta} < 2.8\ \text{cm}$.

7. Summary and Discussion

The first step in this study of overtides was to show that the control run of our high-resolution model of the upper Bay of Fundy (UBoF) agrees well with the overwhelmingly dominant semi-diurnal tides observed in coastal sea level, bottom pressure, and current. The model also agrees well with observations of mean currents. The skill of UBoF is comparable to WebTide, a data-assimilating tidal model that covers the Scotian Shelf and Gulf of Maine, and a significant improvement over GoMSS (Table 2). Good agreement was also found between observations of M_4 currents and predictions by UBoF and WebTide. Both models gave poor predictions of M_4 elevation. This was explained in terms of an error generated in the upper reaches of Cobequid Bay, related to the representation of wetting and drying in the models, that subsequently propagated throughout the model domains as a shallow water wave. A statistical method ("station referencing") was developed to remove this remotely generated signal from the M_4 observations and predictions prior to validation, thereby allowing useful information to be extracted from the M_4 elevations. We anticipate this method has wider applicability to other regions. Using the tidally validated UBoF model, we next addressed the three research questions listed in the Introduction. Our answers are summarized and discussed below.

"How useful are observed overtides in selecting the optimal bathymetry for an ocean model, and constraining the model's parameters? The M_2 tidal amplitude varies by less than ±20% over the upper Bay of Fundy and the phase changes by less than ±20° (Figure 2). The reason is that the length of the Bay is short compared to the tidal wavelength and so the predicted M_2 elevation is controlled primarily by the tidal elevation specified at the open boundary of the model (e.g., Li & O'Donnell, 2005) and not the details of the bathymetry. Snapshots of the predicted M_2 tidal current (not shown) indicate a large scale, approximately rectilinear oscillating flow along the bay that weakens toward the head and is everywhere in quadrature with the M_2 tidal elevation. This flow can be explained, to first order, by simply integrating the continuity equation and calculating the M_2 tidal transport required to balance the change in volume caused by the periodic variation of M_2 tidal elevation. According to this explanation, the M_2 tidal current depends on the bathymetry through variations in cross-sectional area along the Bay.

M_4 varies on spatial scales that are much smaller than the variation of M_2 (compare Figure 2 with Figure 4, and Figure 3 with Figure 5). This is readily explained by the small spatial scale of the nonlinearities that generate the overtides (Figure 9). Based on γ^2 for M_2 and M_4 tides, and mean currents (Figure 10), we selected the publicly available GEBCO gridded bathymetry, supplemented with approximately 10^5 in-situ measurements, as the optimal bathymetry for UBoF. It is the most accurate of the set of bathymetries examined in this study and the higher skill is explained by the improved representation of advection and bottom friction by the model. The M_4 tidal currents were important in reaching this conclusion.

Based on a set of sensitivity studies (see Section 6.3) we showed that, given the limited observations available for the study region, it is challenging to define a "best" set of model parameters for UBoF. However, validation using overtides does provide useful information that leads to stronger constraints on the model parameters.

"How useful are observed overtides in validating model predictions of MDT?" The control run of UBoF predicts a mean sea level difference between Minas Basin and Minas Channel of $\Delta\overline{\eta} = 2.6$ cm. This setup has the opposite sign, and smaller magnitude, than the corresponding prediction by GoMSS ($\Delta\overline{\eta} = -6.1$ cm). Based on the poor predictions of M_4 current and mean current by GoMSS (Table 2), its MDT prediction should also be considered suspect. The skillful predictions of M_4 current and mean current by UBoF show that this model has captured the dominant nonlinear processes in this tidally-dominated region, thereby increasing our confidence in its prediction of MDT.

Our validation approach can also be used in other regions with strong astronomical tides and at least one nonlinear mechanism to generate overtides. Such conditions can be found in many shallow-water coastal zones (e.g., in the vicinity of headlands, narrow tidal straits, and tidal bays and inlets), thereby increasing the applicability of the approach beyond the Bay of Fundy. In addition to validating MDT, the comparison of observed and predicted overtides is also useful in assessing and improving ocean models, in particular their representation of the underlying nonlinear processes responsible for the overtides (e.g., Pingree & Maddock, 1978).

"How useful are observed overtides in designing geodetic and ocean observing systems?" From a geodesist's perspective, a high resolution ocean model, validated using observed overtides and mean currents, can provide guidance in future deployments of tide gauges in support of geoid model validation. Predictions by such models can be used to identify, and thus avoid, regions with highly localized features in MDT that exceed the standard error of the most recent generation of geoid models (3 cm, Huang, 2017). For example, tidal flow around headlands can result in local setdowns of coastal MDT of order $\mathcal{O}$(10 cm) resulting from the combined effect of Bernoulli setdown and the pressure gradient required to balance the mean bottom stress along the coast. Bernoulli setdowns of similar order are also possible in narrow tidal channels like Minas Passage.

From an oceanographer's perspective, the two main advantages of using overtides to validate an ocean model's MDT (and hence its mean state) are (a) the observed record can be relatively short, that is, $\mathcal{O}$(1 month) and (b) its vertical datum does not need to be specified. Reliable observations of mean sea level for MDT validation using the standard geodetic approach require hourly records that are at least several decades in length with continuous vertical datum control (Woodworth et al., 2012). On the negative side, predictions of overtides in sea level can be contaminated by remotely generated errors and care must be taken in the selection of coastal tide gauges and offshore bottom pressure sensors in order to minimize such errors. If the errors propagate as a shallow water wave, their remote effect will have a relatively weak signature in currents compared to sea level. This implies that, in some regions, observed overtides in currents may be more useful than overtides at sea level for model validation.

In the future, it might be possible to supplement the model validation of overtides and MDT in shallow coastal regions using satellite altimetry observations. Currently, these observations are limited by their quality and availability within a distance of about 30 km from the coast (e.g., Andersen & Scharroo, 2011). This distance is much greater than the size of most shallow narrow tidal straits, headlands, and tidal bays and inlets where pronounced overtides and associated changes in MDT are expected to be found. Longer records and ongoing improvements in instrumentation and data processing (e.g., Benveniste et al., 2020; Birol et al., 2017) are expected to weaken this limitation.

Data Availability Statement

All of the code and data required to configure and run the UBoF model are publicly available: NEMO source code (https://www.nemo-ocean.eu/), Webtide for open boundary conditions (https://www.bio.gc.ca/science/research-recherche/ocean/webtide/index-en.php), GEBCO for high-resolution gridded bathymetry (https://www.gebco.net/), and supplementary in-situ bathymetric observations from the Canadian Hydrographic Service. The sea level, bottom pressure and current observations were obtained from individuals and the Marine Environmental Data Section Archive at the Department of Fisheries and Oceans Canada (https://meds-sdmm.dfo-mpo.gc.ca) as described in the text. The tidal analysis of predicted depth-averaged currents was performed using the Python implementation of the UTide package (Codiga, 2011) which is publicly available at https://github.com/wesleybowman/UTide.

Acknowledgments
This work was funded by the Marine Environmental Observation, Prediction and Response (MEOPAR) Network of Canada. CR acknowledges funding from Nova Scotia Graduate Research Scholarship. KRT acknowledges support through the NSERC Discovery Grant program. The authors thank Anna Katavouta, David Greenberg, Shannon Nudds, and Yongsheng Wu for their support and encouragement. The authors also thank the anonymous reviewers for their insightful comments that helped improve the manuscript.

References

Andersen, O. B., & Scharroo, R. (2011). Range and geophysical corrections in coastal regions: And implications for mean sea surface determination. In S. Vignudelli, A. G. Kostianoy, P. Cipollini, & J. Benveniste (Eds.), *Coastal altimetry* (pp. 103–145). Springer. https://doi.org/10.1007/978-3-642-12796-0_5

Aubrey, D. G., & Speer, P. E. (1985). A study of non-linear tidal propagation in shallow inlet/estuarine systems Part I: Observations. *Estuarine, Coastal and Shelf Science*, *21*, 185–205. https://doi.org/10.1016/0272-7714(85)90096-4

Batchelor, G. K. (1967). *An introduction to Fluid dynamics*. Cambridge University Press.

Benveniste, J., Birol, F., Calafat, F., Cazenave, A., Dieng, H., Gouzenes, Y., et al. (2020). Coastal sea level anomalies and associated trends from Jason satellite altimetry over 2008-2010. *Scientific Data*, *7*(1), 357. https://doi.org/10.1038/s41597-020-00694-w

Birol, F., Fuller, N., Lyard, F., Cancet, M., Niño, F., Delebecque, C., et al. (2017). Coastal applications from nadir altimetry: Example of the X-TRACK regional products. *Advances in Space Research*, *59*(4), 936–953. https://doi.org/10.1016/j.asr.2016.11.005

Chassignet, E. P., Hurlburt, H. E., Smedstad, O. M., Halliwell, G. R., Hogan, P. J., Wallcraft, A. J., & Bleck, R. (2007). The HYCOM (HYbrid Coordinate Ocean Model) data assimilative system. *Journal of Marine Systems*, *65*(1–4), 60–83. https://doi.org/10.1016/J.JMARSYS.2005.09.016

Codiga, D. L. (2011). *Unified tidal analysis and prediction using the UTide Matlab functions (Tech. Rep. No. 2011-01)*. Graduate School of Oceanography, University of Rhode Island. https://doi.org/10.13140/RG.2.1.3761.2008

Davies, A. M., & Lawrence, J. (1994). A three-dimensional model of the M_4 tide in the Irish Sea: The importance of open boundary conditions and influence of wind. *Journal of Geophysical Research*, *99*(C8), 16197. https://doi.org/10.1029/94JC00480

Dupont, F., Hannah, C. G., & Greenberg, D. A. (2005). Modelling the sea level of the upper Bay of Fundy. *Atmosphere-Ocean*, *43*(1), 33–47. https://doi.org/10.3137/ao.430103

Dupont, F., Hannah, C. G., Greenberg, D. A., Cherniawsky, J. Y., & Naimie, C. E. (2002). *Modelling system for tides for the Northwest Atlantic coastal ocean* (*Tech. Rep. No. 221*). Bedford Institute of Oceanography.

Foreman, M. G. G., & Henry, R. F. (1989). The harmonic analysis of tidal model time series. *Advances in Water Resources*, *12*(3), 109–120. https://doi.org/10.1016/0309-1708(89)90017-1

Friedrichs, C. T., & Aubrey, D. G. (1988). Non-linear tidal distortion estuaries in shallow well-mixed estuaries: A synthesis. *Estuarine, Coastal and Shelf Science*, *27*(5), 521–545. https://doi.org/10.1016/0272-7714(88)90082-0

Garrett, C. (1972). Tidal resonance in the Bay of Fundy and Gulf of Maine. *Nature*, *238*(5365), 441–443. https://doi.org/10.1038/238441a0

Geyer, W. R., & Signell, R. (1990). Measurements of tidal flow around a headland with a shipboard acoustic Doppler current profiler. *Journal of Geophysical Research*, *95*(C3), 3189. https://doi.org/10.1029/JC095iC03p03189

Greenberg, D. A. (1969). Modification of the M_2 tide due to barriers in the Bay of Fundy. *Journal of the Fisheries Research Board of Canada*, *26*(11), 2775–2783. https://doi.org/10.1139/f69-274

Greenberg, D. A. (1983). Modeling the mean barotropic circulation in the Bay of Fundy and Gulf of Maine. *Journal of Physical Oceanography*, *13*(5), 886–904. https://doi.org/10.1175/1520-0485(1983)013<0886:mtmbci>2.0.co;2

Hasegawa, D., Sheng, J., Greenberg, D. A., & Thompson, K. R. (2011). Far-field effects of tidal energy extraction in the Minas Passage on tidal circulation in the Bay of Fundy and Gulf of Maine using a nested-grid coastal circulation model. *Ocean Dynamics*, *61*(11), 1845–1868. https://doi.org/10.1007/s10236-011-0481-9

Higginson, S., Thompson, K. R., Woodworth, P. L., & Hughes, C. W. (2015). The tilt of mean sea level along the east coast of North America. *Geophysical Research Letters*, *42*(5), 1471–1479. https://doi.org/10.1002/2015GL063186

Huang, J. (2017). Determining coastal mean dynamic topography by geodetic methods. *Geophysical Research Letters*, *44*(21), 11125–11128. https://doi.org/10.1002/2017GL076020

Hughes, C. W., & Bingham, R. J. (2006). An oceanographer's guide to GOCE and the geoid. *Ocean Science Discussions*, *3*(5), 1543–1568.

Hughes, C. W., Fukumori, I., Griffies, S. M., Huthnance, J. M., Minobe, S., Spence, P., & Wise, A. (2019). Sea level and the role of coastal trapped waves in mediating the influence of the open ocean on the coast. *Surveys in Geophysics*, *40*(6), 1467–1492. https://doi.org/10.1007/s10712-019-09535-x

Karsten, R. H., McMillan, J. M., Lickley, M. J., & Haynes, R. D. (2008). Assessment of tidal current energy in the Minas Passage, Bay of Fundy. *Proceedings of the Institution of Mechanical Engineers - Part A: Journal of Power and Energy*, *222*(5), 493–507. https://doi.org/10.1243/09576509JPE555

Katavouta, A., & Thompson, K. R. (2016). Downscaling ocean conditions with application to the Gulf of Maine, Scotian Shelf and adjacent deep ocean. *Ocean Modelling*, *104*(Supplement C), 54–72. https://doi.org/10.1016/j.ocemod.2016.05.007

Katavouta, A., Thompson, K. R., Lu, Y., & Loder, J. W. (2016). Interaction between the tidal and seasonal variability of the Gulf of Maine and Scotian shelf region. *Journal of Physical Oceanography*, *46*(11), 3279–3298. https://doi.org/10.1175/JPO-D-15-0091.1

Large, G., & Yeager, S. (2004). Diurnal to decadal global forcing for ocean and sea-ice models: The data sets and flux climatologies (*Tech. Rep. Nos. NCAR/TN-460+STR)*. University Corporation for Atmospheric Research.

Le Provost, C. (1991). Generation of overtides and compound tides (review). In B. B. Parker (Ed.), *Tidal hydrodynamics* (pp. 269–295). Wiley.

Lentz, S. J., & Fewings, M. R. (2012). The wind- and wave-driven inner-shelf circulation. *Annual Review of Marine Science*, *4*(1), 317–343. https://doi.org/10.1146/annurev-marine-120709-142745

Levier, B., Tréguier, A.-M., Madec, G., & Garnier, V. (2007). *Free surface and variable volume in the NEMO code* (Tech. Rep.). Brest: Ifremer.

Lin, H., Thompson, K. R., Huang, J., & Véronneau, M. (2015). Tilt of mean sea level along the Pacific coasts of North America and Japan. *Journal of Geophysical Research: Oceans*, *120*(10), 6815–6828. https://doi.org/10.1002/2015JC010920

Li, C., & O'Donnell, J. (1997). Tidally driven residual circulation in shallow estuaries with lateral depth variation. *Journal of Geophysical Research: Oceans*, *102*(C13), 27915–27929. https://doi.org/10.1029/97JC02330

Li, C., & O'Donnell, J. (2005). The effect of channel length on the residual circulation in tidally dominated channels. *Journal of Physical Oceanography*, *35*(10), 1826–1840. https://doi.org/10.1175/JPO2804.1

Lyard, F., Lefevre, F., Letellier, T., & Francis, O. (2006). Modelling the global ocean tides: Modern insights from FES2004. *Ocean Dynamics*, *56*(5–6), 394–415. https://doi.org/10.1007/s10236-006-0086-x

Madec, G., Romain, B.-B., Pierre-Antoine, B., Clément, B., Diego, B., Daley, C., et al. (2017). NEMO ocean engine version 3.6 stable (*Tech. Rep. No. 27*). Pôle de modélisation de l'Institut Pierre-Simon Laplace (IPSL). https://doi.org/10.5281/zenodo.1472492

Maraldi, C., Chanut, J., Levier, B., Ayoub, N., De Mey, P., Reffray, G., et al. (2013). NEMO on the shelf: Assessment of the Iberia-Biscay-Ireland configuration. *Ocean Science*, *9*(4), 745–771. https://doi.org/10.5194/os-9-745-2013

Mardell, G. T., & Pingree, R. D. (1981). Half-wave rectification of tidal vorticity near headlands as determined from current meter measurements. *Oceanologica Acta*, *4*(1), 63–68.

Munk, W. H. (1950). On the wind-driven ocean circulation. *Journal of Meteorology*, *7*(2), 80–93. https://doi.org/10.1175/1520-0469(1950)007<0080:otwdoc>2.0.co;2

Parker, B. B. (1991). The relative importance of the various nonlinear mechanisms in a wide range of tidal interactions (Review). In B. B. Parker (Ed.), *Tidal hydrodynamics* (pp. 237–268). Wiley.

Pingree, R. D., Griffiths, D. K., & Maddock, L. (1984). Quarter diurnal shelf resonances and tidal bed stress in the English Channel. *Continental Shelf Research*, *3*(3), 267–289. https://doi.org/10.1016/0278-4343(84)90012-8

Pingree, R. D., & Maddock, L. (1977). Tidal eddies and coastal discharge. *Journal of the Marine Biological Association of the United Kingdom*, *57*(03), 869. https://doi.org/10.1017/S0025315400025224

Pingree, R. D., & Maddock, L. (1978). The M_4 tide in the English Channel derived from a nonlinear model of the M_2 tide. *Deep-Sea Research*, *25*(1), 53–63. https://doi.org/10.1016/s0146-6291(21)00006-0

Proudman, J. (1953). *Dynamical Oceanography*. Methuen.

Robinson, I. (1983). Chapter 7: Tidally induced residual flows. In B. Johns (Ed.), *Physical Oceanography of coastal and Shelf seas* (Vol. 35, pp. 321–356). Elsevier. https://doi.org/10.1016/s0422-9894(08)70505-1

Rodi, W. (1987). Examples of calculation methods for flow and mixing in stratified fluids. *Journal of Geophysical Research*, *92*(C5). 5305. https://doi.org/10.1029/JC092iC05p05305

Saha, S., Moorthi, S., Pan, H.-L., Wu, X., Wang, J., Nadiga, S., & Goldberg, M. (2010). The NCEP climate forecast system Reanalysis. *Bulletin of the American Meteorological Society*, *91*(8), 1015–1058. https://doi.org/10.1175/2010BAMS3001.1

Signell, R. P., & Geyer, W. R. (1991). Transient eddy formation around headlands. *Journal of Geophysical Research: Oceans*, *96*(C2), 2561–2575. https://doi.org/10.1029/90JC02029

Speer, P. E., & Aubrey, D. G. (1985). A study of non-linear tidal propagation in shallow inlet/estuarine systems Part II: Theory. *Estuarine, Coastal and Shelf Science*, *12*, 207–224. https://doi.org/10.1016/0272-7714(85)90097-6

Speer, P. E., Aubrey, D. G., & Friedrichs, C. T. (1991). Nonlinear hydrodynamics in shallow tidal inlet/bay systems. In *Tidal hydrodynamics* (pp. 321–339).

Stewart, R. W. (1989). The no-slip constraint and ocean models. *Atmosphere-Ocean*, *27*(3), 542–552. https://doi.org/10.1080/07055900.1989.9649351

Stommel, H. (1948). The westward intensification of wind-driven ocean currents. *Transactions - American Geophysical Union*, *29*(2). 202. https://doi.org/10.1029/TR029i002p00202

Tee, K. T. (1976). Tide-induced residual current, a 2-D nonlinear numerical tidal model. *Journal of Marine Research*, *34*, 603–628.

Tee, K. T. (1977). Tide-Induced residual current—Verification of a numerical model. *Journal of Physical Oceanography*, *7*(3), 396–402. https://doi.org/10.1175/1520-0485(1977)007<0396:tircoa>2.0.co;2

Thompson, K. R., Lazier, J. R. N., & Taylor, B. (1986). Wind-forced changes in Labrador current transport. *Journal of Geophysical Research*, *91*(C12), 14261. https://doi.org/10.1029/JC091iC12p14261

Umlauf, L., & Burchard, H. (2003). A generic length-scale equation for geophysical turbulence models. *Journal of Marine Research*, *61*(2), 235–265. https://doi.org/10.1357/002224003322005087

Umlauf, L., & Burchard, H. (2005). Second-order turbulence closure models for geophysical boundary layers. A review of recent work. *Continental Shelf Research*, *25*(7–8), 795–827. https://doi.org/10.1016/J.CSR.2004.08.004

Weatherall, P., Marks, K. M., Jakobsson, M., Schmitt, T., Tani, S., Arndt, J. E., & Wigley, R. (2015). A new digital bathymetric model of the world's oceans. *Earth and Space Science*, *2*(8), 331–345. https://doi.org/10.1002/2015EA000107

Woodworth, P. L., Hughes, C. W., Bingham, R. J., & Gruber, T. (2012). Towards worldwide height system unification using ocean information. *Journal of Geodetic Science*, *2*(4), 302–318. https://doi.org/10.2478/v10156-012-0004-8

Wu, Y., Chaffey, J., Greenberg, D. A., Colbo, K., & Smith, P. C. (2011). Tidally-induced sediment transport patterns in the upper Bay of Fundy: A numerical study. *Continental Shelf Research*, *31*(19), 2041–2053. https://doi.org/10.1016/j.csr.2011.10.009